

## THE OPTX PROJECT V: IDENTIFYING DISTANT AGNS<sup>1</sup>

L. TROUILLE<sup>2</sup>, A. J. BARGER<sup>3,4,5</sup>, AND C. TREMONTI<sup>3</sup>

ACCEPTED TO APJ: *September 30, 2011*

### ABSTRACT

The Baldwin, Phillips, and Terlevich emission-line ratio diagnostic ([OIII]/H $\beta$  versus [NII]/H $\alpha$ , hereafter BPT diagram) efficiently separates galaxies whose signal is dominated by star formation (BPT-SF) from those dominated by AGN activity (BPT-AGN). Yet this BPT diagram is limited to  $z < 0.5$ , the redshift at which [NII] $\lambda$ 6584 leaves the optical spectral window. Using the Sloan Digital Sky Survey (SDSS), we construct a new diagnostic, or TBT diagram, that is based on rest-frame  $g - z$  color, [NeIII] $\lambda$ 3869, and [OII] $\lambda$  $\lambda$ 3726 + 3729 and can be used for galaxies out to  $z < 1.4$ . The TBT diagram identifies 98.7% of the SDSS BPT-AGN as TBT-AGN and 97% of the SDSS BPT-SF as TBT-SF. Furthermore, it identifies 97% of the OPTX *Chandra* X-ray selected AGNs as TBT-AGN. This is in contrast to the BPT diagram, which misidentifies 20% of X-ray selected AGNs as BPT-SF. We use the GOODS-N and Lockman Hole galaxy samples, with their accompanying deep *Chandra* imaging, to perform X-ray and infrared stacking analyses to further validate our TBT-AGN and TBT-SF selections; that is, we verify the dominance of AGN activity in the former and star formation activity in the latter. Finally, we address the inclusion of the majority of the BPT-comp (sources lying between the BPT-SF and BPT-AGN regimes) in our TBT-AGN regime. We find that the stacked BPT-comp source is X-ray hard ( $\langle \Gamma_{\text{eff}} \rangle = 1.0_{-0.4}^{+0.4}$ ) and has a high X-ray luminosity to total infrared luminosity ratio. This suggests that, on average, the X-ray signal in BPT-comp is dominated by obscured or low accretion rate AGN activity rather than by star formation, supporting their inclusion in the TBT-AGN regime.

*Subject headings:* cosmology: observations — galaxies: active — galaxies: nuclei — galaxies: Seyfert — galaxies: distances and redshifts — X-rays: galaxies

### 1. INTRODUCTION

The most commonly used optical emission-line diagnostic for separating star-forming galaxies from type II Active Galactic Nuclei (AGNs) relies on [OIII] $\lambda$ 5007/H $\beta$  versus [NII] $\lambda$ 6584/H $\alpha$  (hereafter, BPT diagram – Baldwin et al. 1981; Veilleux & Osterbrock 1987). The basic idea is that the emission lines in star-forming galaxies are powered by massive stars, so there is a well-defined upper limit on the intensities of the collisionally excited lines relative to the recombination lines (such as H $\alpha$  or H $\beta$ ). In contrast, AGNs are powered by a source of far more energetic photons, making the collisionally excited lines more intense relative to the recombination lines. Two demarcations are commonly used for identifying AGN-dominated galaxies versus star formation dominated galaxies – (1) the Kewley et al. (2001) theoretical division between galaxies whose extreme ultraviolet (EUV) ionizing radiation field is dominated by an AGN (> 50%) and those dominated by star formation

and (2) the Kauffmann et al. (2003) empirical demarcation based on the location of the Sloan Digital Sky Survey (SDSS; York et al. 2000) star-forming galaxies. Galaxies that lie between these two curves are often referred to as composite galaxies. Hereafter, we refer to these categories as BPT-AGN, BPT-SF, and BPT-comp.

The BPT diagram is limited in its use with optical spectra to galaxies with  $z < 0.5$  (the redshift at which [NII] leaves the optical spectral window). A number of groups have tried to extend optical emission line diagnostics to higher redshifts by only using lines at the blue end of the spectrum. Lamareille (2010) replaced [NII]/H $\alpha$  with [OII] $\lambda$ 3726 +  $\lambda$ 3729/H $\beta$ , creating the ‘blue diagram’, which can be used to classify galaxies out to  $z < 0.9$  (see also Tresse et al. 1996; Rola et al. 1997; Lamareille et al. 2004). They find that this diagnostic is very successful at identifying star-forming galaxies (with > 99% of the BPT-SF still classified as SF-dominated) but that it requires complementary diagnostics to robustly classify BPT-AGN (see Marocco et al. 2011). We also note that [OII] and H $\beta$  are relatively distant in wavelength, requiring more careful calibration and extinction corrections.

Recently, Yan et al. (2011) and Juneau et al. (2011) introduced the CEx and MEx diagnostics, respectively, in which they replaced [NII]/H $\alpha$  with rest-frame  $U - B$  color (CEx) or with stellar mass (MEx; see also Weiner et al. 2007). Both diagnostics recover the BPT-AGN classification very well, with 95.7% and > 99% of the BPT-AGN still classified as AGNs in the CEx and MEx diagnostics, respectively. However, because these diagnostics rely on H $\beta$  at  $\lambda$ 4861 Å, their use with optical spectra is limited to  $z < 1$ .

<sup>1</sup> Some of the data presented herein were obtained at the W. M. Keck Observatory, which is operated as a scientific partnership among the California Institute of Technology, the University of California, and the National Aeronautics and Space Administration. The observatory was made possible by the generous financial support of the W. M. Keck Foundation.

<sup>2</sup> Center for Interdisciplinary Exploration and Research in Astrophysics (CIERA) and Department of Physics and Astronomy, 2145 Sheridan Road, Evanston, IL 60208

<sup>3</sup> Department of Astronomy, University of Wisconsin-Madison, 475 N. Charter Street, Madison, WI 53706

<sup>4</sup> Department of Physics and Astronomy, University of Hawaii, 2505 Correa Road, Honolulu, HI 96822

<sup>5</sup> Institute for Astronomy, University of Hawaii, 2680 Woodlawn Drive, Honolulu, HI 96822

At higher redshifts the Stasińska et al. (2006) DEW diagnostic, based on  $D_n[4000]$ ,  $[\text{NeIII}]\lambda 3869$ , and  $[\text{OII}]$  (see also Rola et al. 1997), can be used with optical spectra out to  $z < 1.4$ , at which point the lines move into the infrared. While these emission lines are not as strong as  $[\text{OIII}]$  and  $\text{H}\beta$ , their ratio is the only choice for pushing optical spectra to these higher redshifts.  $[\text{NeIII}]$  emission indicates the presence of highly ionized gas and is much stronger than  $[\text{OII}]$  in high-excitation AGNs. However, because  $D_n[4000]$  requires a sufficiently high signal-to-noise continuum (i.e., using SDSS, we find that the uncertainty on  $D_n[4000]$  ranges from 5% at  $SN/\text{\AA} = 5$  to 25% at  $SN/\text{\AA} = 1$ ; see also Cardiel et al. 1998) and requires the survey to be spectrophotometrically calibrated, its usage with distant galaxies is limited.

In this article we examine whether rest-frame  $g - z$  color, which requires near-infrared imaging at the higher redshifts, is a compelling replacement for  $D_n[4000]$ . While the ratio of  $[\text{NeIII}]/[\text{OII}]$  alone effectively separates metal-rich star-forming galaxies from AGNs, metal-poor star-forming galaxies have high values of  $[\text{NeIII}]/[\text{OII}]$  (as a result of less line blanketing enabling a harder stellar radiation field). Fortunately, metal-poor galaxies also tend to be bluer (see Fig. 7 in Tremonti et al. 2004), so we can use their color to distinguish them from AGNs (which tend to be bulge dominated and redder, see Yan et al. 2011). We refer to this new diagnostic as the TBT diagram.

We first establish the reliability of the TBT diagnostic in reproducing the BPT classifications at low redshifts using SDSS, the largest spectroscopic sample to date of emission-line galaxies. We then test the TBT diagnostic at higher redshifts using the highly spectroscopically complete OPTX X-ray selected sample of AGNs (Trouille et al. 2008, 2009; Trouille & Barger 2010). The misidentification of X-ray selected AGNs as SF-dominated galaxies is a potential issue for all optical emission-line diagnostic diagrams. In Trouille & Barger (2010) we found that  $\sim 20\%$  of the  $L_X > 10^{42} \text{ erg s}^{-1}$  *Chandra* X-ray selected AGNs in our OPTX sample that have  $[\text{OIII}]$ ,  $\text{H}\beta$ ,  $[\text{NII}]$ , and  $\text{H}\alpha$  fluxes with signal-to-noise greater than five are misidentified by the BPT diagram as BPT-SF (see also Winter et al. 2010 for evidence of this in the *Swift* BAT sample and Bongiorno et al. 2010 for evidence of this in the XMM-COSMOS sample). Existing high-redshift optical emission-line diagnostics also misidentify a significant fraction of X-ray selected AGNs, e.g.,  $\sim 8\%$  and  $\sim 22\%$  of X-ray selected AGNs in the MEx and CEx diagrams lie in the MEx-SF and CEx-SF regimes, respectively.

Stacking techniques have been widely used in X-ray astronomy to study the average properties of source populations selected to have certain well-defined properties and which are too X-ray faint to be detected individually (e.g., Brandt et al. 2001; Alexander et al. 2001; Hornschemeier et al. 2002; Nandra et al. 2002; Georgakakis et al. 2003; Laird et al. 2005; Lehmer et al. 2005, 2008; Treister et al. 2009). As a proof-of-concept of the TBT diagnostic, we perform an X-ray stacking analysis of the TBT-SF and TBT-AGN in the highly spectroscopically complete Great Observatories Origins Deep Survey North (GOODS-N; Giavalisco et al. 2004)

with accompanying *Chandra* Deep Field North (CDFN; Alexander et al. 2003) imaging to determine whether they are, on average, X-ray soft or X-ray hard.

An X-ray hard source is indicative of obscured AGN activity or the presence of high-mass X-ray binaries (HMXBs) associated with ongoing star formation. An X-ray soft source is indicative of unobscured AGN activity or the presence of low-mass X-ray binaries (LMXBs) associated with old stellar populations. In order to distinguish between these scenarios, we perform an infrared (IR) stacking analysis using the *Spitzer Space Telescope*  $24\mu\text{m}$  data. Numerous studies have found a relation between the X-ray and IR luminosities for star-forming galaxies and for AGNs (Ptak et al. 2003; Persic et al. 2004; Alexander et al. 2005; Teng et al. 2005; Georgakakis et al. 2007). We compare the X-ray and IR luminosities for our stacked TBT-SF and stacked TBT-AGN with the results from these studies to verify the dominance of star formation activity in the former and AGN activity in the latter.

We then perform X-ray and IR stacking analyses of the BPT categories to confirm the presence of AGN activity in BPT-comp, as suggested by the TBT diagnostic. In most optical emission-line diagnostics, the BPT-comp lie in a transition region or within the SF-dominated regime. For example, Kewley et al. (2006) find that BPT-comp are indistinguishable from HII regions and are significantly distinct from Seyferts in an  $[\text{OIII}]/[\text{OII}]$  versus  $[\text{OI}]/\text{H}\alpha$  plot. In both the ‘blue diagram’ and the CEx diagnostic, the majority of BPT-comp lie within their SF-dominated regimes ( $\sim 83\%$  and  $\sim 75\%$ , respectively). In contrast, the bulk of BPT-comp lie within our TBT-AGN regime (see also the MEx diagnostic). Because BPT-comp are a significant percentage of the overall low-redshift emission-line galaxy population (e.g., in SDSS<sup>6</sup>, BPT-SF, BPT-comp, and BPT-AGN comprise 69%, 20%, and 11%, respectively, of the overall population), inclusion or exclusion of BPT-comp in AGN samples can have an important impact on results. In order to have the necessary statistics required to do a robust stacking analysis, we combine our GOODS-N galaxy sample with galaxy samples from two Lockman Hole (LH) fields, all of which have deep *Chandra* imaging.

The structure of the paper is as follows. In Section 2 we briefly describe the SDSS sample, our OPTX X-ray selected sample of AGNs, and our optical spectroscopic samples of the GOODS-N/LH fields. In Section 3 we use the SDSS sample to calibrate our TBT diagnostic to match the BPT diagram. In Section 4 we determine how well our TBT-AGN selection matches with an X-ray selection of AGNs. In Section 5 we do X-ray and IR stacking analyses to verify the reliability of our TBT-AGN and TBT-SF classes. In Section 6 we do X-ray and IR stacking analyses on our BPT-comp to determine whether the implications of the TBT diagnostic with respect to the dominance of AGN activity in BPT-comp are confirmed. In Section 7 we compare our TBT diagnostic to other diagnostics for separating star-forming galaxies from AGNs. In Section 8 we summarize our results.

<sup>6</sup> Here we have restricted the SDSS DR8 sample to emission-line galaxies whose  $[\text{NII}]$ ,  $\text{H}\alpha$ ,  $[\text{OIII}]$ , and  $\text{H}\beta$  fluxes have a signal-to-noise ratio greater than five.

All magnitudes are in the AB magnitude system. We assume  $\Omega_M = 0.3$ ,  $\Omega_\Lambda = 0.7$ , and  $H_0 = 70 \text{ km s}^{-1} \text{ Mpc}^{-1}$ .

## 2. SAMPLE

### 2.1. SDSS: Low-Redshift Galaxy Sample

SDSS has obtained deep, multi-color images covering more than a quarter of the sky with follow-up spectroscopy of over a million objects. Here we use the SDSS spectroscopic data from Data Release 8 (DR8; Aihara et al. 2011). We use the emission-line fluxes measured by the MPA-JHU group as described in Section 4.3 of the data release paper. These fluxes are estimated from simultaneous Gaussian fits to the continuum subtracted spectra to account for stellar absorption and line blending. DR8 provides spectra for 868,492 different galaxies. The SDSS spectral range is 3800 – 9200 Å. Since the [OII] line lies at 3726 Å and the [NII] line lies at 6584 Å, we limit our SDSS samples to galaxies with  $0.02 < z < 0.35$ . Our SDSS BPT sample consists of the 243,865 SDSS galaxies that have H $\alpha$ , [NII], H $\beta$ , and [OIII] fluxes with signal-to-noise ratio (SNR) greater than five (out of the 818,333 spectra for different galaxies in the DR8 sample). Of these SDSS BPT galaxies, 23,048 also have both [NeIII] and [OII] fluxes with SNR > 5. We refer to these as our SDSS TBT sample.

### 2.2. OPTX: X-ray Selected Sample of AGNs

The OPTX sample consists of 1789 X-ray sources in two intermediate depth wide-field surveys in the Lockman Hole region of low galactic column density and one deep pencil-beam survey (CDFN; Brandt et al. 2001; Alexander et al. 2003). The Lockman Hole fields are the *Chandra* Large Area Synoptic X-ray Survey (CLASXS; Yang et al. 2004) and the *Chandra* Lockman Area North Survey (CLANS; Trouille et al. 2008, 2009; Wilkes et al. 2009). We have spectroscopically observed 84% of the OPTX sources using the DEep Imaging Multi-Object Spectrograph (DEIMOS; Faber et al. 2003) on the Keck II 10 m telescope and the HYDRA multi-object spectrograph on the WIYN 3.5 m telescope (for details of the observations and reduction process, see Trouille et al. 2008).

In Trouille et al. (2008, 2009) we used the X-ray fluxes and spectroscopic redshifts to calculate rest-frame 2 – 8 keV luminosities,  $L_X$ . At  $z < 3$  (which is all we consider in this paper), we calculated the luminosities from the observed-frame 2 – 8 keV fluxes, assuming an intrinsic X-ray spectral index of  $\Gamma = 1.8$ . That is,  $L_X = f \times 4\pi d_L^2 \times k$ -correction, where for  $z < 3$ ,  $k$ -correction =  $(1+z)^{\Gamma-2}$  and  $f = f_{2-8 \text{ keV}}$ . Using the individual X-ray spectral indices (e.g.,  $\langle \Gamma \rangle \sim 1.75$  with a dispersion of  $\approx 0.33$  derived by Tozzi et al. 2006 for the X-ray bright CDFS sources), rather than the universal X-ray spectral index of  $\Gamma = 1.8$  adopted here, to calculate the  $k$ -corrections would result in only a small difference (an average factor of 0.9) in the rest-frame luminosities. We have not corrected the X-ray luminosities for absorption since these corrections are small in the 2 – 8 keV band (e.g., Barger et al. 2002), and we are only using the X-ray luminosities to identify sources as X-ray AGNs.

In the following, we limit our study to the 561 OPTX X-ray sources with spectroscopic redshifts, whose 2 –

8 keV flux has a significance greater than  $3\sigma$ , and whose  $L_X > 10^{42} \text{ erg s}^{-1}$  (247, 163, and 151 sources from the CLANS, CLASXS, and CDFN fields, respectively).  $L_X > 10^{42} \text{ erg s}^{-1}$  is a commonly used conservative threshold for AGN activity (Hornschemeier et al. 2001; Barger et al. 2002; Szokoly et al. 2004; Silverman et al. 2005; Coil et al. 2009) that is based on energetic grounds (Zezas et al. 1998; Moran et al. 1999). Using the calibration by Ranalli et al. (2003), one would need a star formation rate (SFR) of  $200 M_\odot \text{ yr}^{-1}$  to produce enough X-ray luminosity from non-AGNs to cross this threshold. In Trouille & Barger (2010) we found a < 5% contamination rate of our OPTX sample by sources with SFR >  $200 M_\odot \text{ yr}^{-1}$ . We determined this using the Magnelli et al. (2009) space densities at a range of redshifts for ultraluminous infrared galaxies (ULIRGs) with estimated SFR >  $172 M_\odot$ .

Our study focuses on optical emission-line ratio diagnostics based on flux ratios. We compute the relative line fluxes from the spectra using the Tremonti et al. (2004) software. In brief, we subtract the stellar continuum and absorption lines by fitting a linear combination of single stellar population models of different ages (Bruzual & Charlot 2003). We remove any remaining residuals from the continuum using a sliding 250 Å median. The relative line fluxes and errors are estimated from simultaneous Gaussian fits to the continuum subtracted spectra.

Our DEIMOS spectra are of high quality from  $\sim 4800 \text{ Å}$  to  $\sim 9300 \text{ Å}$ , such that the [OII] and [NeIII] lines lie within our spectral window from  $z \sim 0.3 - 1.4$ . Of our 561 OPTX X-ray sources, 197 are non-broad-line AGNs (FWHM <  $2000 \text{ km s}^{-1}$ ; hereafter non-BLAGNs) and lie within this redshift range. We only include non-BLAGNs in this analysis, since the narrow lines in BLAGNs are overwhelmed by the emission from the broad-line region. We identify 103 OPTX X-ray selected AGNs that have [NeIII] and [OII] fluxes with SNR > 5.

### 2.3. GOODS-N/LH: Higher-Redshift Galaxy Sample

Each of the three OPTX fields is the focus of a comprehensive spectroscopic follow-up of all galaxies in the field. The CDFN encompasses the intensively studied GOODS-N field, which we describe in more detail below. The CLANS and CLASXS fields reside in the Lockman Hole (LH) region of low Galactic column density.

A random spectroscopic sample of 3082  $K_{s,AB} < 21.5$  galaxies in these two LH fields was obtained using DEIMOS on Keck II (L. Cowie, priv. comm.). We hereafter refer to this combined sample as the LH galaxy sample.

The GOODS-N field has among the deepest images ever obtained in a number of bandpasses, including the *Chandra* 2 Ms CDFN image. It also has been the target of extensive spectroscopic observations over the years (e.g., Cohen et al. 2000; Wirth et al. 2004; Cowie et al. 2004; Barger et al. 2008; Cooper et al. 2011). With its high optical spectroscopic completeness and deep X-ray coverage, the GOODS-N catalog provides an ideal sample for studying the average X-ray properties of optically selected samples of AGNs.

Barger et al. (2008) presented a highly complete spectroscopic survey of the GOODS-N field. Over the years a

number of groups have made observations of this region, first primarily using the Low-Resolution Imaging Spectrograph (LRIS; Oke et al. 1995) on the Keck I 10 m telescope and later using DEIMOS. Barger et al. added to these samples by observing all missing or unidentified galaxies to date with DEIMOS. In order to provide a uniform spectral database, they also re-observed sources where the original spectra were of poor quality or where previous redshifts were obtained with instruments other than DEIMOS. The redshift identifications are now greater than 90% complete to magnitudes of  $F435W_{AB} = 24.5$  and  $K_{s,AB} = 21.5$  and to  $24 \mu\text{m}$  fluxes of  $250 \mu\text{Jy}$ . The final Barger et al. catalog provides spectroscopic redshifts for 2710 galaxies in this field.

We compute the relative line fluxes for the relevant emission lines in the combined GOODS-N/LH galaxy sample using the same method and software as described for the OPTX X-ray sample above. To create our GOODS-N/LH BPT diagram, we use the 727 sources that have  $[\text{OIII}]$ ,  $\text{H}\beta$ ,  $[\text{NII}]$ , and  $\text{H}\alpha$  fluxes with  $\text{SNR} > 5$ . For our GOODS-N TBT diagram, we use the 670 sources that have  $[\text{NeIII}]$  and  $[\text{OII}]$  fluxes with  $\text{SNR} > 5$ . As discussed in the previous subsection, because of the DEIMOS spectral window, the GOODS-N sources plotted in our TBT diagnostic have a redshift range from  $z = 0.3 - 1.4$ .

In Figure 1 we show the redshift distributions (out to  $z = 1.5$ ) for the SDSS, GOODS-N, LH, and OPTX samples. The large SDSS sample has a median redshift of  $\langle z \rangle \sim 0.1$ , whereas the GOODS-N, LH, and OPTX surveys allow us to test our TBT diagnostic out to  $z = 1.4$ .

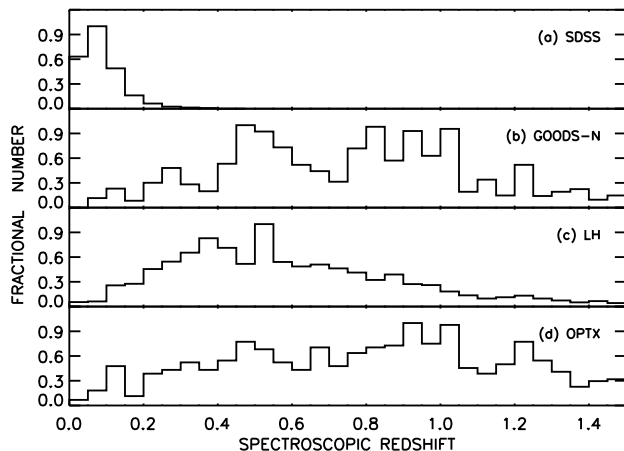


FIG. 1.— Spectroscopic redshift distribution out to  $z = 1.5$  for (a) the SDSS BPT sample, (b) the GOODS-N galaxy survey, (c) the LH galaxy survey, and (d) the OPTX survey. The different redshift ranges seen in (a)-(c) reflect the magnitude limits of the different surveys.

#### 2.4. Rest-frame $g, z$ Magnitudes

We have  $u, g, r, i, z$  magnitudes for the SDSS galaxies (Abazajian et al. 2009),  $g, r, i, z, J$ ,  $H, K_s$  magnitudes for the OPTX AGNs and LH galaxies (Trouille et al. 2008; Keenan et al. 2010), and  $B, V, R, I, Z, J, H, K_s$  magnitudes for the GOODS-N galaxies (Giavalisco et al. 2004; Barger et al. 2008; Keenan et al. 2010). We transform the observed pho-

tometry into  $g$  and  $z$  magnitudes at  $z = 0$  using `kcorrect v4.1.4` (Blanton & Roweis 2007). For  $z = 1.4$  sources, the  $g$ -band ( $\sim 0.5 \mu\text{m}$ ) redshifts into the  $J$ -band ( $\sim 1.2 \mu\text{m}$ ) and the  $z$ -band ( $\sim 0.9 \mu\text{m}$ ) redshifts into the  $K$ -band ( $\sim 2.2 \mu\text{m}$ ). As a result, fields with extensive photometric coverage use observed-frame bandpasses that are very close to the rest-frame  $g$ - and  $z$ -bandpasses of interest, and so the  $k$ -corrections are small. For our TBT diagnostic, we subtract the rest-frame  $z$ -band from the rest-frame  $g$ -band to obtain the rest-frame  $g - z$  color; hereafter,  ${}^{0.0}(g - z)$ .

To determine the error associated with the  ${}^{0.0}(g - z)$  color for each sample, we randomly alter the magnitudes by an amount consistent with the photometric uncertainties and re-run the Blanton & Roweis (2007) software. We then determine the  $1 \sigma$  standard deviation on  $\Delta = {}^{0.0}(g - z)_{\text{original}} - {}^{0.0}(g - z)_{\text{random}}$ . For our SDSS sample,  $\sigma_{\Delta} = 0.21$ . For our GOODS-N/LH sample,  $\sigma_{\Delta} = 0.07$ . The high-quality photometry and extensive coverage of our GOODS-N/LH fields ensures these low  $k$ -correction errors.

Chilingarian et al. (2010) compare the Blanton & Roweis (2007) `kcorrect` code with their own to explore the systematic error associated with  $k$ -correction software. For  $k$ -corrected optical colors (e.g.,  ${}^{0.0}[g - r]$ ,  ${}^{0.0}[r - z]$ ), the differences between the resulting colors from the two codes are relatively small ( $\sim 0.05$  or less). Therefore, for our study, systematic errors are not significant. However, we note here for completeness that for  $k$ -corrected colors in which one band is in the rest-frame IR (e.g.,  ${}^{0.0}[r - H]$ ,  ${}^{0.0}[r - K]$ ), the differences can be significant ( $\sim 0.15$ ; see their Fig. 7), and the systematic error need be taken into account.

### 3. A NEW $Z < 1.4$ EMISSION-LINE RATIO DIAGNOSTIC

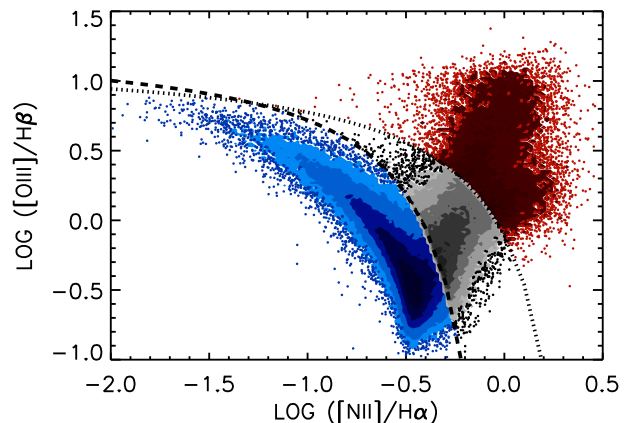


FIG. 2.— BPT diagram -  $\log([\text{NII}]/\text{H}\alpha)$  vs.  $\log([\text{OIII}]/\text{H}\beta)$  - for the SDSS galaxies that have  $[\text{OIII}]$ ,  $\text{H}\beta$ ,  $[\text{NII}]$ , and  $\text{H}\alpha$  with  $\text{SNR} > 5$ . The dashed curve shows the Kauffmann et al. (2003) empirical division between star-forming galaxies and AGNs. The dotted curve shows the Kewley et al. (2001) theoretical division. As discussed in the text, we represent the SDSS data using a combination of a two-dimensional histogram and plotted points. BPT-SF are shown in blue, BPT-comp in gray, and BPT-AGN in red.

Figure 2 shows the BPT diagram (based on flux ratios of the specified lines) applied to our SDSS BPT

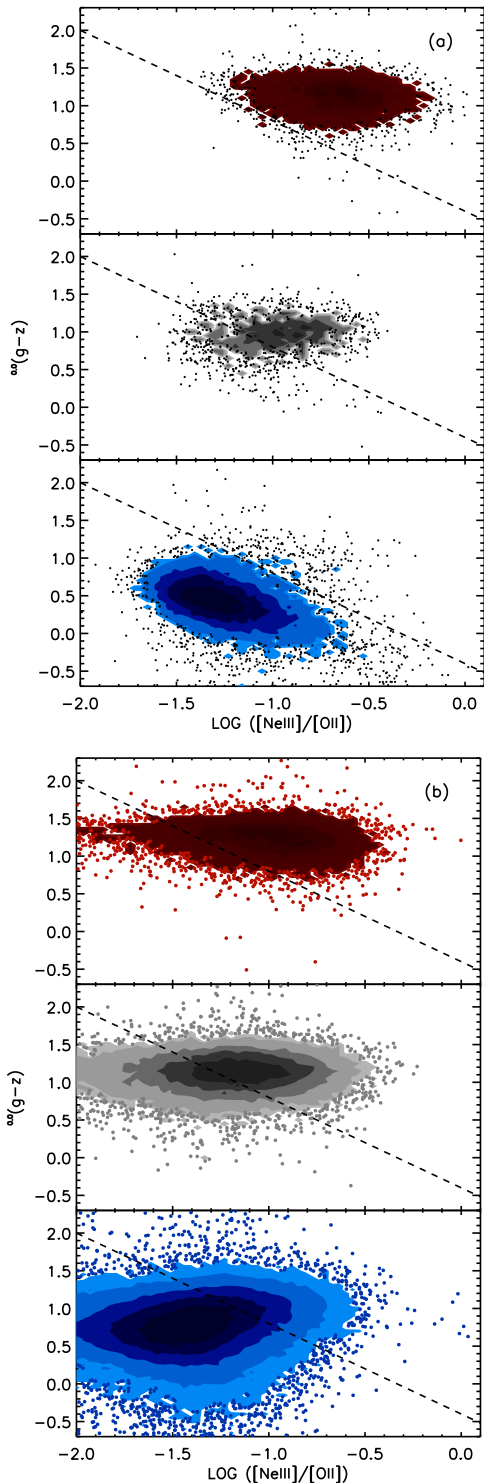


FIG. 3.— (a) TBT diagram  $-^{0.0}(g-z)$  color vs.  $\log([\text{NeIII}]/[\text{OII}])$  – for the SDSS galaxies that have  $[\text{OIII}]$ ,  $\text{H}\beta$ ,  $[\text{NII}]$ ,  $\text{H}\alpha$ ,  $[\text{NeIII}]$ , and  $[\text{OII}]$  fluxes with  $\text{SNR} > 5$ . The top, middle, and bottom panels show the positions of the BPT-AGN, BPT-comp, and BPT-SF, respectively. The dashed line provides the empirical separation maximizing the fraction of BPT-AGN to total population in the upper-right of the diagram (see Eq. 1). (b) Same as (a) but for SDSS galaxies that have  $[\text{OIII}]$ ,  $\text{H}\beta$ ,  $[\text{NII}]$ ,  $\text{H}\alpha$ , and  $[\text{OII}]$  with  $\text{SNR} > 5$ , but  $[\text{NeIII}]$  has  $\text{SNR} < 5$ . For the 15% with  $[\text{NeIII}] \leq 0$ , we set  $[\text{NeIII}]$  equal to the  $1\sigma$  error.

sample. The dotted curve indicates the Kewley et al. (2001) theoretical division and the dashed curve indicates the Kauffmann et al. (2003) empirical division between AGNs and star-forming galaxies, as discussed in the Introduction. In this and subsequent figures we represent the SDSS data using a combination of a two-dimensional histogram and plotted points. We histogram the data where more than four data points fall in an individual pixel (the size of the pixel is determined by dividing the plot into  $150 \times 150$  bins) and plot it as individual points otherwise. The histograms have been square root scaled for better visibility. Each step in contour level represents 20% fewer sources. The darkest contours correspond to 391 sources, 42 sources, and 151 sources for the BPT-SF, BPT-AGN, and BPT-comp, respectively.

We find that 69% of our SDSS BPT sample lie below the Kauffmann et al. (2003) division, in the BPT-SF regime, 11% lie above the Kewley et al. (2001) division, in the BPT-AGN regime, and 20% lie in between the two divisions, in the BPT-comp regime. If instead we apply the BPT diagnostic to our SDSS TBT sample (i.e., SDSS galaxies that have  $[\text{OIII}]$ ,  $\text{H}\beta$ ,  $[\text{NII}]$ ,  $\text{H}\alpha$ ,  $[\text{NeIII}]$ , and  $[\text{OII}]$  fluxes with  $\text{SNR} > 5$ ), we find that 60% are BPT-SF, 32% are BPT-AGN, and 8% are BPT-comp.

The BPT diagram can only be used to identify AGNs out to  $z = 0.5$ , the redshift at which  $[\text{NII}]$  leaves the optical spectral window. The ratio of  $[\text{NeIII}]$  to  $[\text{OII}]$  is a good candidate for pushing optical narrow emission-line ratio diagnostics to higher redshifts because both lines are relatively strong, lie in the blue end of the spectrum (measurable in optical spectra out to  $z < 1.4$ ), and are close in wavelength (thus avoiding reddening effect issues). Furthermore,  $[\text{NeIII}]$  has a significantly higher ionization potential (63.45 eV) than  $[\text{OII}]$  (35.12 eV). As a result, the  $[\text{NeIII}]/[\text{OII}]$  ratio is higher in AGNs than in star-forming galaxies. We also note that the ionization potential for  $[\text{NeIII}]$  is significantly higher than for  $[\text{OIII}]$ , whose ionization potential is 54.94 eV. In Section 7 we discuss how AGN selection using a  $[\text{NeIII}]$ -based diagnostic may be more discerning than one based on  $[\text{OIII}]$  as a result of this higher ionization potential (requiring a harder ionizing flux).

In Figure 3(a) we plot our TBT diagnostic  $-^{0.0}(g-z)$  color versus  $\log([\text{NeIII}]/[\text{OII}])$  – for our SDSS TBT sample, color-coded according to the BPT classifications in Figure 2. The top, middle, and bottom panels show the locations of the BPT-AGN, BPT-comp, and BPT-SF, respectively. The darkest contours correspond to 71 sources, 16 sources, and 68 sources for the BPT-AGN, BPT-comp, and BPT-SF, respectively. The BPT-SF show a trend with color in that the bluer BPT-SF exhibit higher values of  $[\text{NeIII}]/[\text{OII}]$ . This provides a separation in color-space between the BPT-AGN and the BPT-SF with high values of  $[\text{NeIII}]/[\text{OII}]$ . This trend with color is likely due to the fact that bluer galaxies are more metal poor (see Fig. 7 in Tremonti et al. 2004) and hence have harder stellar radiation fields (higher  $[\text{NeIII}]/[\text{OII}]$ ; Shi et al. 2007). On the other hand, few BPT-AGN reside in very blue galaxies. As discussed in detail in Section 3.3 of Yan et al. (2011), nearly all BPT-AGN are found in red galaxies or in galaxies with intermediate colors between red and blue.

The dashed line designates

$$^{0.0}(g-z) = -1.2 \times \log([\text{NeIII}]/[\text{OII}]) - 0.4, \quad (1)$$

our empirical separation maximizing the fraction of BPT-AGN to total population in the upper-right of the diagram. Hereafter, we refer to the sources in the upper-right (lower-left) of our TBT diagnostic as TBT-AGN (TBT-SF).

We find that 98.7% of the BPT-AGN lie in the TBT-AGN regime and 97.2% of the BPT-SF lie in the TBT-SF regime. Likewise, we find that only 3.5% of the sources in the TBT-AGN regime are BPT-SF and 1% of the sources in the TBT-SF regime are BPT-AGN. The BPT-comp lie on either side of the division, with 68.6% in the TBT-AGN regime. Overall the BPT-comp constitute 5% and 16% of the TBT-SF and TBT-AGN, respectively.

There are 200,712 galaxies in our SDSS BPT sample that have [OII] with SNR > 5 but [NeIII] with SNR < 5. In Figure 3(b) we show the TBT diagram for these sources. For the 15% with [NeIII] ≤ 0, we set [NeIII] equal to the 1 σ error. The darkest contours correspond to 94 sources, 170 sources, and 546 sources for the BPT-AGN, BPT-comp, and BPT-SF, respectively. We find that ~85% of the BPT-SF lie within the TBT-SF regime, ~86% of the BPT-AGN lie within the TBT-AGN regime, and ~62% of the BPT-comp lie within the TBT-AGN regime. The trends follow those for our SDSS TBT sample. The 8% of SDSS BPT galaxies for which neither [OII] nor [NeIII] has SNR > 5 and the < 1% of SDSS BPT galaxies for which [NeIII] has SNR > 5 but [OII] has SNR < 5 are not considered here.

We have trained our TBT diagnostic on the SDSS galaxies, which have ⟨z⟩ ~ 0.1. Because our TBT diagnostic can be used with optical spectra out to z = 1.4, we examine the impact of metallicity evolution with redshift on our empirical separation between TBT-AGN and TBT-SF. Galaxy metallicities decrease by a factor of ~0.3 dex between the local value and the value at z ~ 2 (Erb et al. 2006; see also Cowie & Barger 2008; Kewley & Ellison 2008; Zahid et al. 2011). For an M<sub>star</sub> = 10<sup>10</sup>M<sub>⊙</sub> galaxy, this corresponds to a shift from 12 + log(O/H) = 8.6 to 8.3 (note that more massive galaxies undergo less metallicity evolution). Using the Shi et al. (2007) relation between metallicity and log([NeIII]/[OII]), we find that, in this case, log([NeIII]/[OII]) shifts by only ~20%, from -0.89 to -0.72. Applying this 20% increase in the ratio of [NeIII] to [OII] to all SDSS BPT-SF, we find that an additional 5% move to the TBT-AGN regime. This corresponds to an increase of only 5.5% in the number of TBT-AGN that are BPT-SF. Similarly, there is only a 1.8% increase in the number of TBT-AGN that are BPT-comp. Because the impact is relatively small, in this article we do not consider any metallicity evolution with redshift in our empirical separation between TBT-SF and TBT-AGN.

We also considered the impact of color evolution on our TBT diagnostic. At higher redshifts, galaxies are bluer as a result of higher specific star formation rates. Purely passive evolution models (Bruzual & Charlot 2003) with an instantaneous burst and a Chabrier (2003) initial mass function predict a Δ<sup>0.0</sup>(g-z) ~ 0.24 between z = 0 and 1.4, for a formation redshift of 5. Applying this color evolution to all SDSS BPT-SF, the impact is in our favor.

The BPT-SF move down the y-axis in our TBT diagnostic to lie even further below our empirical separation, in the TBT-SF regime. Applying this color evolution to all SDSS BPT-AGN, we find that an additional 3.6% move to the TBT-SF regime. This corresponds to an increase of 2.7% in the number of TBT-SF that are BPT-AGN. Similarly, there is only a 2.9% increase in the number of TBT-SF that are BPT-comp. Because the impact is small, in this article we do not consider any color evolution with redshift in our empirical separation between TBT-SF and TBT-AGN.

#### 4. COMPARING THE TBT DIAGNOSTIC WITH AN X-RAY SELECTION OF AGNS

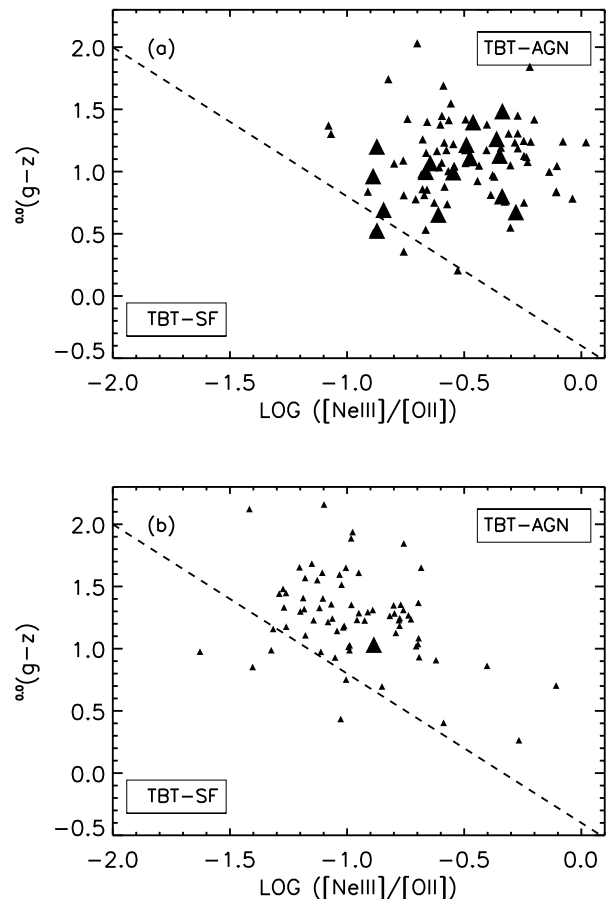


FIG. 4.— (a) TBT diagram  $^{0.0}(g-z)$  color vs.  $\log([\text{NeIII}]/[\text{OII}])$  – for the X-ray selected non-BLAGNs in our OPTX sample with  $0.3 < z < 1.4$  for which the [NeIII] and [OII] fluxes have a SNR > 5. *Small black triangles*—non-BLAGNs with  $10^{42} < L_X < 10^{44}$  erg s<sup>-1</sup>. *Large black triangles*—non-BLAGNs with  $L_X > 10^{44}$  erg s<sup>-1</sup>. The dashed line provides the empirical separation maximizing the fraction of BPT-AGN to total population in the upper-right of the diagram (see Figure 3 and Eq. 1). (b) Same as (a) but for the OPTX X-ray selected non-BLAGNs for which [OII] has a SNR > 5 but [NeIII] has a SNR < 5. For the 6% with [NeIII] ≤ 0, we set [NeIII] equal to the 1 σ error.

In Trouille & Barger (2010) we found that only a little over half (52%) of the X-ray selected non-BLAGNs in our OPTX sample lie in the BPT-AGN regime of the BPT diagram. These sources form a sequence similar to that



of the BPT-AGN, emerging from the HII region sequence and extending to the upper-right hand side of the BPT diagram.

Of the X-ray selected non-BLAGNs in our OPTX sample, 20% are misidentified as BPT-SF, i.e., as pure star-forming galaxies (Trouille & Barger 2010; see also Winter et al. 2010 for evidence of this in the *Swift* BAT sample). Increased extinction does not account for these. Instead, in Trouille & Barger (2010) we note that these misidentified sources have lower  $L_{\text{[OIII]}}/L_X$  ratios than those that lie in the BPT-AGN regime. We postulate that the low forbidden emission line strengths in the misidentified sources are a result of the complexity of the structure of the narrow-line region, which causes ionizing photons from the central engine to not be absorbed.

The misidentification of X-ray selected AGNs as star-forming galaxies is a potential issue for all optical emission-line diagnostic diagrams, including our TBT diagram. In Figure 4(a) we plot the TBT diagram  $-^{0.0}(g-z)$  color versus  $\log([\text{NeIII}]/[\text{OII}])$  for the  $0.3 < z < 1.4$  X-ray selected non-BLAGNs in our OPTX sample that have  $[\text{NeIII}]$  and  $[\text{OII}]$  with  $\text{SNR} > 5$ . We find that 97% (100/103) of our X-ray selected AGNs lie in the TBT-AGN regime. Thus, the TBT diagnostic does a much better job of correctly identifying X-ray selected AGNs than the BPT diagnostic, misidentifying only 3% as TBT-SF compared to the BPT diagnostic’s misidentification of 20% as BPT-SF.

As mentioned in Section 2.2, there are 94  $0.3 < z < 1.4$  OPTX non-BLAGNs that do not fulfill the criteria of having both  $[\text{NeIII}]$  and  $[\text{OII}]$  with  $\text{SNR} > 5$ . Sixteen of these have neither  $[\text{OII}]$  nor  $[\text{NeIII}]$  with a  $\text{SNR} > 5$ . In Figure 4(b) we show the remaining 78 OPTX X-ray selected non-BLAGNs for which  $[\text{OII}]$  has a  $\text{SNR} > 5$  but  $[\text{NeIII}]$  has a  $\text{SNR} < 5$ . No sources have only  $[\text{NeIII}]$  with a  $\text{SNR} > 5$ . We find that 92% (72/78) lie in the TBT-AGN regime. This supports our results for the OPTX sources in which both  $[\text{NeIII}]$  and  $[\text{OII}]$  have a  $\text{SNR} > 5$ .

## 5. VERIFICATION OF THE TBT DIAGNOSTIC: STACKING ANALYSES

The GOODS-N sample of spectroscopically observed galaxies with deep *Chandra* and *Spitzer* imaging out to  $z = 1.4$  provides an ideal pilot for confirming the dominance of AGN activity in the TBT-AGN and star formation activity in the TBT-SF.

Figure 5 shows our TBT diagnostic for the 642  $0.3 < z \leq 1.4$  GOODS-N sources for which the  $[\text{NeIII}]$  and  $[\text{OII}]$  fluxes have a  $\text{SNR} > 5$ . We have excluded sources with broadened emission lines ( $\text{FWHM} > 2000 \text{ km s}^{-1}$ ) from this analysis. The dashed line indicates our empirical division between the TBT-AGN and TBT-SF (see Figure 3 and Eq. 1). We find that 189 GOODS-N sources lie in the TBT-AGN regime, corresponding to a space density of  $4.6 \times 10^{-5} \text{ Mpc}^{-3}$  optically selected GOODS-N TBT-AGN.

There are 11 GOODS-N sources in our TBT diagram that are cross-listed as non-BLAGNs in the CDFN catalog with  $L_X > 10^{42} \text{ erg s}^{-1}$  (black triangles). As discussed in Section 4, our TBT diagnostic has a much lower rate of misidentifying X-ray selected AGNs as star-forming galaxies than the BPT diagnostic ( $\sim 3\%$  versus 20%). We use our OPTX X-ray selected sample of AGNs for that analysis. Since the GOODS-N field lies within

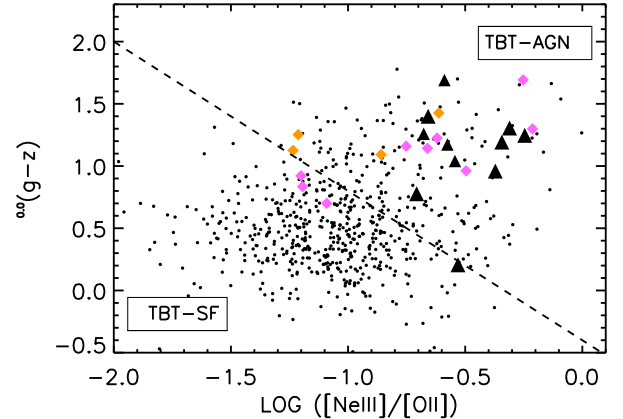


FIG. 5.— TBT diagram  $-^{0.0}(g-z)$  color vs.  $\log([\text{NeIII}]/[\text{OII}])$  for the GOODS-N  $0.3 < z < 1.4$  sources for which the  $[\text{NeIII}]$  and  $[\text{OII}]$  fluxes have a  $\text{SNR} > 5$ . *Large black triangles*—non-BLAGNs cross-listed in the *Chandra* catalog with  $L_X > 10^{42} \text{ erg s}^{-1}$ . *Orange diamonds*—non-BLAGNs cross-listed in the *Chandra* catalog, but with  $L_X < 10^{42} \text{ erg s}^{-1}$ . These sources are significantly detected in both the 0.5–2 keV band and 2–8 keV bands. *Magenta diamonds*—non-BLAGNs cross-listed in the *Chandra* catalog, but with  $L_X < 10^{42} \text{ erg s}^{-1}$ . These sources are significantly detected in the 0.5–2 keV band but not the 2–8 keV band. *Black circles*—remaining sources. The dashed line provides the empirical separation maximizing the fraction of BPT-AGN to total population in the upper-right of the diagram (see Figure 3 and Eq. 1).

the CDFN, one of our OPTX fields, it is no surprise that only one of the  $L_X > 10^{42} \text{ erg s}^{-1}$  non-BLAGNs (black triangles) in Figure 5 is misidentified as a TBT-SF.

In the following section we perform X-ray and IR stacking analyses in order to investigate whether the remaining  $L_X < 10^{42} \text{ erg s}^{-1}$  TBT-AGN harbor obscured AGN activity, verifying the validity of our TBT-AGN selection. We also perform stacking analyses of our TBT-SF in order to verify the dominance of star formation activity in these sources. The effective X-ray spectral slope ( $\Gamma_{\text{eff}}$ ; derived from the ratio of the 2–8 keV band to the 0.5–2 keV band) is indicative of different source types. Unobscured AGNs exhibit  $\Gamma_{\text{eff}} \geq 1.7$ . In obscured AGNs, photoelectric absorption of X-ray soft photons by neutral gas along the line of sight causes a flattening of the slope, such that  $\Gamma_{\text{eff}} < 1.7$  (although see Trouille et al. 2009 for a discussion of discrepancies between X-ray and optical spectral type). At the same time, X-ray binaries exhibit a range in X-ray spectral slopes. LMXBs, which are associated with old stellar populations, tend to be softer in X-rays, with  $\Gamma > 1.7$ . HMXBs, which are associated with ongoing star formation, tend to be harder in X-rays, with  $\Gamma = 0.5 - 1$  (Colbert et al. 2004). See Fabbiano (2006) and Remillard & McClintock (2006) for detailed reviews of X-ray binary populations. In order to distinguish between these scenarios, we perform an IR stacking analysis in Section 5.2.

We restrict our analysis to lower redshift sources ( $z < 0.7$ ) in order to not be misled by the automatic softening of the effective X-ray spectral slope as one observes to higher redshifts (i.e., as the redshift increases, the 0.5–2 keV and 2–8 keV bands are sampling higher energies whose photons can more easily penetrate obscuring material).

### 5.1. X-ray Stacking

Quantitatively, if stacking a sample of ‘ $n$ ’ objects yields ‘ $N_s$ ’ counts in a signal aperture of area ‘ $A_s$ ’ and ‘ $N_b$ ’ smoothed background counts in that same area ‘ $A_s$ ’, then the mean number of source counts per object in the signal region is

$$\langle N \rangle_{src} = \frac{1}{n} [N_s - N_b]. \quad (2)$$

We obtain an estimate of the mean spectral slope of the detected signal by performing the stacking in two energy bands, soft (0.5 – 2 keV) and hard (2 – 8 keV), and deriving an effective power-law photon index,  $\langle \Gamma_{\text{eff}} \rangle$ .

Here we use the STACKFAST X-ray stacking program (Hickox et al. 2007). In STACKFAST, ‘ $A_s$ ’ is defined as the area enclosed within  $r_{90}$  from the source position, where  $r_{90}$  is an approximation of the 90% point-spread function (PSF) energy encircled radius at 1.5 keV, and varies as<sup>1</sup>:

$$r_{90} = 1'' + 10''(\theta/10')^2, \quad (3)$$

with  $\theta$  equal to the off-axis angle. In order to maximize the number of source counts, rather than limiting the stacking to only the central 6’ as in Hickox et al. (2007), we use the central 10’ around the pointing center for each observation.

A few bright sources would dominate our estimate of the mean spectral shape, so we exclude from our analysis sources that lie close to or are associated with a known X-ray detected source, hereafter called coincidental contaminants (see also Hickox et al. 2007; Georgantopoulos et al. 2008; Fiore et al. 2008). To this end, we first applied a mask to all known X-ray detected source positions. We used  $3 \times r_{90}$  (see Eq. 3) as the mask aperture radius.

We cross reference the ‘ $A_s$ ’ for our sources of interest with the X-ray photon locations from each *Chandra* pointing (i.e., each OBSID event file). We then create smoothed 0.5 – 2 keV and 2 – 8 keV background maps using the CIAO WAVDETECT task and determine the background counts within the same ‘ $A_s$ ’. Subtracting this background and dividing by the number of sources being stacked, we obtain the average X-ray signal in counts per source. We create exposure maps using custom routines (A. Vikhlinin, private communication) and determine the total exposure time for each source being stacked. Dividing the total counts in the stacked source by the total exposure time, we derive the average count rate (counts per second) for the stacked source. We use the ratio of the 2 – 8 keV count rate to the 0.5 – 2 keV count rate to derive  $\langle \Gamma_{\text{eff}} \rangle$ .

Count uncertainties are calculated using the approximation  $\sqrt{X + 0.75} + 1$ , where  $X$  is the number of counts in a given band (Gehrels 1986). We set a significance threshold of  $3 \sigma$ . Uncertainties in the hardness ratio and  $\langle \Gamma_{\text{eff}} \rangle$  are derived by propagating these count rate errors.

Table 1 shows the results from our stacking analysis for the GOODS-N TBT-SF and TBT-AGN. Column 2 lists the total number of sources in each of these categories. Column 3 provides the total number of sources used in the stacking analysis, after excluding individually X-ray detected sources and coincidental contaminants.

Columns 4 and 5 state fluxes and detection significance for the given X-ray band. We consider that stacked sources with  $< 3 \sigma$  detection are not significantly detected. Column 6 provides the  $\langle \Gamma_{\text{eff}} \rangle$  value for the stacked source. In column 7 we list the volume-weighted redshift for the stacked source and in column 8 we list the derived 2 – 8 keV luminosity based on the  $f_{2-8 \text{ keV}}$  and the volume-weighted redshift.

We provide specifics for each category in the following subsections.

#### 5.1.1. TBT-SF

There are 155  $z < 0.7$  GOODS-N TBT-SF. As discussed above, we restrict our analysis to these lower redshifts in order to not be misled by the automatic softening of the effective X-ray spectral slope as one observes to higher redshift. Only one of these  $z < 0.7$  GOODS-N TBT-SF is directly X-ray detected, and then only in the 0.5 – 2 keV band. Using the 2 – 8 keV flux limit for the CDFN image (see Table 2), we determine an upper limit to its hardness ratio and find that it is X-ray soft, with  $\Gamma > 1.7$ .

After excluding this known X-ray source, as well as coincidental contaminants, we use the STACKFAST program to determine the average X-ray signal in the remaining 148 TBT-SF. The stacked source is significantly detected in the 0.5 – 2 keV band ( $4.7 \sigma$ ) but not in the 2 – 8 keV band ( $2.2 \sigma$ ). We find a  $\langle \Gamma_{\text{eff}} \rangle = 1.5^{+0.7}_{-0.4}$ , although we caution that this is based on a low-significance 2 – 8 keV signal. Given the large uncertainties, the stacked source could be X-ray soft ( $\Gamma > 1.7$ ).

#### 5.1.2. TBT-AGN

There are 72  $z < 0.7$  GOODS-N TBT-AGN. Six are directly X-ray detected in both the 0.5 – 2 keV and 2 – 8 keV bands. Three of these are obvious X-ray selected AGNs with  $L_X > 10^{42} \text{ erg s}^{-1}$ . The three remaining X-ray detected sources have  $L_X < 10^{42} \text{ erg s}^{-1}$ . All three are X-ray hard, with  $\Gamma < 1.4$ .

After excluding these known X-ray sources, as well as coincidental contaminants, we use the STACKFAST program to determine the average X-ray signal in the remaining 54 TBT-AGN. The stacked source is significantly detected in both bands ( $5.4 \sigma$  in the 0.5 – 2 keV band and  $4.0 \sigma$  in the 2 – 8 keV band). We find a  $\langle \Gamma_{\text{eff}} \rangle = 1.0^{+0.3}_{-0.3}$ , consistent with being X-ray hard ( $\Gamma < 1.4$ ).

#### 5.1.3. Monte-Carlo Simulation

We carried out a series of Monte Carlo (MC) stacking simulations to assess false-detection probabilities empirically. For each category we performed 1000 trials and used the same number of stacked sources and the same procedure as in the original stacking, albeit with random RA and Dec positions.

In Section 5.1.1 we found that the TBT-SF are significantly detected in the 0.5 – 2 keV band but not in the 2 – 8 keV band. In Section 5.1.2 we found that the TBT-AGN are significantly detected in both the 0.5 – 2 keV and 2 – 8 keV bands.

Our MC simulations yield a 0.1% probability of generating the observed 0.5 – 2 keV flux for our stacked TBT-SF source and a 52% probability of generating the

<sup>1</sup> <http://cxc.harvard.edu/proposer/POG>



TABLE 1  
 TBT X-RAY STACKING ANALYSIS RESULTS

Category (1)	Total # (2)	# used in stack (3)	$f_{0.5-2 \text{ keV}}^a$ (4)	$f_{2-8 \text{ keV}}^a$ (5)	$\langle \Gamma_{\text{eff}} \rangle$ (6)	$z^b$ (7)	$\log L_{2-8 \text{ keV}} [\text{erg s}^{-1}]$ (8)
TBT-SF <sup>c</sup>	155	148	$0.62 \pm 0.13$ (4.7 $\sigma$ )	$2.50 \pm 1.1$ (2.2 $\sigma$ )	$1.5_{-0.4}^{+0.7d}$	0.58	40.53 <sup>d</sup>
TBT-AGN <sup>c</sup>	72	54	$1.13 \pm 0.2$ (5.4 $\sigma$ )	$5.87 \pm 1.4$ (4 $\sigma$ )	$1.0_{-0.3}^{+0.3}$	0.58	40.86

<sup>a</sup>In units of  $10^{-17} \text{ erg cm}^{-2} \text{ s}^{-1}$ .

<sup>b</sup>Volume-weighted redshift for the stacked source.

<sup>c</sup>Only including sources with  $z < 0.7$ .

<sup>d</sup>We caution that this is based on a low significance 2 – 8 keV signal.

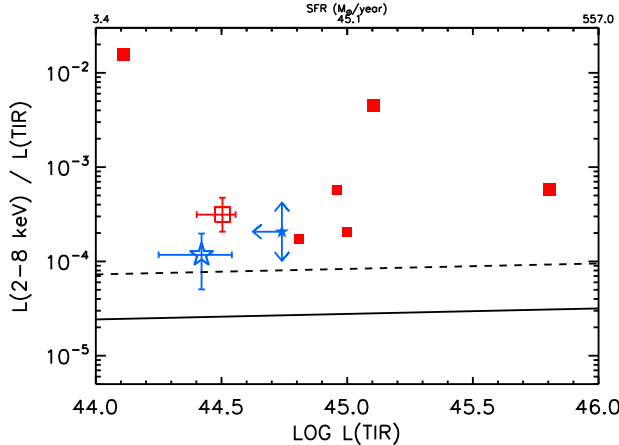


FIG. 6.—  $L_{2-8 \text{ keV}}/L_{\text{TIR}}$  versus  $\log L_{\text{TIR}}$  for our  $0.3 < z < 0.7$  GOODS-N galaxies that have [NeIII] and [OII] fluxes with  $\text{SNR} > 5$ . Red filled squares – directly X-ray detected TBT-AGN. Large (small) symbols indicate sources with  $L_X > 10^{42} \text{ erg s}^{-1}$  ( $L_X < 10^{42} \text{ erg s}^{-1}$ ). Blue filled star – directly X-ray detected TBT-SF. The downward pointing arrow indicates that the source is undetected in the 2 – 8 keV band and is assigned the 2 – 8 keV flux limit (see Table 2). The upward and leftward pointing arrows indicate that the source is undetected in the *Spitzer* 24 $\mu\text{m}$  image and is assigned the 24 $\mu\text{m}$  flux limit (see Table 2). Red open square – stacked TBT-AGN, excluding directly X-ray detected sources. Blue open star – stacked TBT-SF, excluding directly X-ray detected sources. Solid line – expected ratio for the HMXB population in a galaxy with the given SFR (see top axis), according to Persic et al. (2004); dashed line – expected ratio for the overall star formation occurring in a galaxy with the given SFR, according to Mineo et al. (2011).

observed 2 – 8 keV flux. Our MC analysis confirms that the TBT-SF clearly have an excess of 0.5 – 2 keV counts, well above those we obtain randomly. The 2 – 8 keV signal is within the noise. Thus, the observed X-ray softness in our TBT-SF appears to be a reliable result.

Our MC simulations for the TBT-AGN yield a 0% probability that we would see the observed 0.5 – 2 keV flux or the observed 2 – 8 keV flux. Our MC analysis confirms we are recovering a real signal in both bands. None of our MC simulations for the TBT-AGN result in both the 0.5 – 2 keV and 2 – 8 keV bands detected at a 3  $\sigma$  level or greater. In other words, there is a  $\sim 0\%$  false-alarm rate for our stacked TBT-AGN signal. Thus, the observed X-ray hardness in our TBT-AGN appears to be a reliable result.

## 5.2. IR Stacking

In Section 5.1 we derived the average X-ray properties for the GOODS-N TBT-SF and TBT-AGN using an X-ray stacking analysis. The stacked TBT-AGN source was significantly detected in both the 0.5–2 keV and 2–8 keV bands and was quite X-ray hard, with  $\langle \Gamma_{\text{eff}} \rangle = 1.0_{-0.3}^{+0.3}$ .

 TABLE 2  
 FLUX LIMITS

<i>Chandra</i> 2 – 8 keV Image	Flux Limit ( $\text{erg cm}^{-2} \text{ s}^{-1}$ )
CDFN	$1.5 \times 10^{-16}$
CLANS	$3.5 \times 10^{-15}$
CLASXS	$3.5 \times 10^{-15}$
<i>Spitzer</i> 24 $\mu\text{m}$ Image	Flux Limit ( $\mu\text{Jy}$ )
GOODS-N	75
LH <sup>a</sup>	150

<sup>a</sup>Includes both the CLANS and CLASXS fields.

This X-ray hard signal could be due either to AGN activity with obscuration or HMXBs associated with ongoing star formation.

Numerous studies have found that in star-forming galaxies without an AGN, the total X-ray luminosity correlates with the SFR (Nandra et al. 2002; Bauer et al. 2002; Ranalli et al. 2003; Grimm et al. 2003; Colbert et al. 2004; Persic et al. 2004; Hornschemeier et al. 2005; Persic & Rephaeli 2007; Rovilos et al. 2009). Furthermore, David et al. (1992) found a linear relation between the far-infrared (FIR) luminosity and the 0.5 – 4.5 keV luminosities for a sample of starburst galaxies observed by *Einstein* (see also Fabbiano & Shapley 2002). Ranalli et al. (2003) extended this study to the 2 – 10 keV band using the *ASCA* and *BeppoSAX* satellites. Persic et al. (2004) determined the relation between the X-ray and FIR luminosities for both the full contribution from star formation activity and for HMXBs alone. A number of groups have shown that AGNs and AGN-starburst composite galaxies lie above these relations (Ptak et al. 2003; Alexander et al. 2005; Teng et al. 2005; Georgakakis et al. 2007). The additional X-ray luminosity is attributed to AGN activity in these galaxies.

Following these previous studies, here we use the IR properties of our TBT-AGN to determine whether the X-ray hard signal is due to AGN activity with obscuration or HMXBs. We also check whether the X-ray soft signal in our TBT-SF is consistent with pure star-forming galaxies. In Trouille et al. (2009) we determined the *Spitzer* 24 $\mu\text{m}$  fluxes and luminosities for our OPTX X-ray selected AGNs. We follow the same procedure here to determine  $f_{24\mu\text{m}}$  and  $L_{24\mu\text{m}}$  for our GOODS-N galaxies.

To determine  $f_{24\mu\text{m}}$  for our stacked TBT-AGN and stacked TBT-SF, we use the publicly available IAS Stacking Library IDL software (Bethérmin et al. 2010). The IAS Stacking software uses a DAOPHOT-type photometry IDL procedure, APER, with a preset PSF for the *Spitzer* 24 $\mu\text{m}$  band (13'' for the object aperture and sky radii of 20'' – 32''). A median stacking is preferable to mean stacking because the median analysis is more sta-

ble and robust to small numbers of bright sources. Using the volume-weighted redshift for our stacked source, we transform  $f_{24\mu\text{m}}$  into  $L_{24\mu\text{m}}$ . We then use the Rieke et al. (2009) eq. A6 to transform  $L_{24\mu\text{m}}$  into the total infrared luminosity,  $L_{\text{TIR}}$ .

The IAS Stacking software provides the  $1\sigma$  standard deviation on the stacked flux. However, given that the *Spitzer* image resolution is low, we need to consider the likelihood of misidentifications and overlap. To assess how well this  $1\sigma$  standard deviation reflects the contamination from spurious signals, we carry out a series of Monte Carlo stacking. We perform 1000 trials and use the same number of stacked sources and follow the same procedure as in the original stacking. The only difference is that we use random RA and Dec positions. For both our stacked TBT-AGN and our stacked TBT-SF,  $> 99\%$  of our simulations result in stacked fluxes less than our  $1\sigma$  error. While  $< 10\%$  of the random RA, Dec positions in each simulation do overlap with real  $24\mu\text{m}$  sources (as expected given the low image resolution), because we use a median stacking, these spuriously high fluxes are excluded from the stacked signal.

In Figure 6 we plot the ratio of the X-ray to total IR luminosities,  $L_X/L_{\text{TIR}}$ , versus  $L_{\text{TIR}}$  for our TBT categories. The top axis shows the associated SFR for a given  $L_{\text{TIR}}$ , following Rieke et al. (2009). The solid line shows the expected ratio derived by Persic et al. (2004) for the HMXB population in a galaxy with the given SFR. The dashed line shows the Mineo et al. (2011) expected ratio for all star formation activity in a galaxy with the given SFR. The stacked TBT-SF (blue open star) was significantly detected in the  $0.5 - 2$  keV band ( $4.7\sigma$ ) but not in the  $2 - 8$  keV band ( $2.2\sigma$ ). Nonetheless, we use the derived  $L_X$  from the stacking analysis (see Table 1) and determine the  $1\sigma$  error on  $L_X/L_{\text{TIR}}$  by propagating the errors on both the stacked X-ray and IR signal. The stacked TBT-SF  $L_X/L_{\text{TIR}}$  is consistent with that expected for pure star-forming galaxies. This corroborates what we find for the one individually X-ray detected TBT-SF (blue filled star). Since this source is undetected in both the *Spitzer*  $24\mu\text{m}$  image and the CDFN  $2 - 8$  keV image, we assign it the flux limits for these images (see Table 2) and use the arrows to designate it as corresponding to upper limits. Given these uncertainties, its  $L_X/L_{\text{TIR}}$  is not inconsistent with pure star-forming galaxies.

The three X-ray detected TBT-AGN with  $L_X > 10^{42}$  erg s $^{-1}$  (large red filled squares) and the three X-ray detected TBT-AGN with  $L_X < 10^{42}$  erg s $^{-1}$  (small red filled squares) lie clearly above the expected range for  $L_X/L_{\text{TIR}}$  for pure star-forming galaxies. The stacked TBT-AGN (red open square) also lies well above this range. We determine the  $1\sigma$  error on  $L_X/L_{\text{TIR}}$  for the stacked source by propagating the errors on both the stacked X-ray and IR signal. We find that the stacked TBT-AGN lies  $> 3\sigma$  above the expected range for  $L_X/L_{\text{TIR}}$  for pure star-forming galaxies, supporting our hypothesis that, on average, TBT-AGN harbor AGN activity.

## 6. BPT DIAGNOSTIC: STACKING ANALYSES

In Section 3 we found that the majority of the SDSS BPT-comp lie within the TBT-AGN regime. Here our primary goal is to do X-ray and IR stacking analyses to

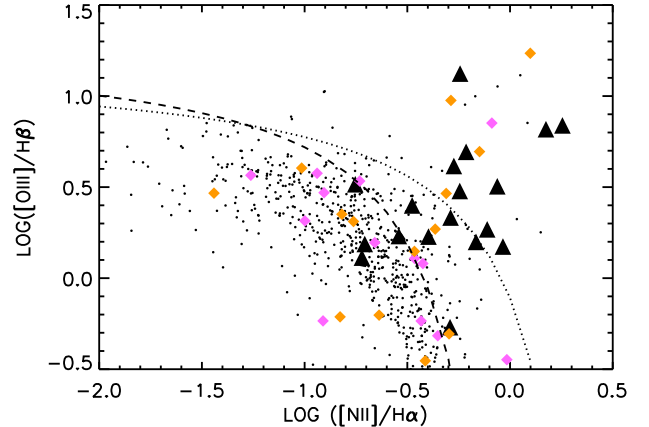


FIG. 7.— (a) BPT diagram for the GOODS-N/LH  $z < 0.5$  sources that have [OIII], H $\beta$ , [NII], and H $\alpha$  fluxes with SNR  $> 5$ . *Large black triangles*—non-BLAGNs cross-listed in the *Chandra* catalog with  $L_X > 10^{42}$  erg s $^{-1}$ . *Orange diamonds*—non-BLAGNs cross-listed in the *Chandra* catalog, but with  $L_X < 10^{42}$  erg s $^{-1}$ . These sources are significantly detected in both the  $0.5 - 2$  keV band and  $2 - 8$  keV bands. *Magenta diamonds*—non-BLAGNs cross-listed in the *Chandra* catalog, but with  $L_X < 10^{42}$  erg s $^{-1}$ . These sources are significantly detected in the  $0.5 - 2$  keV band but not the  $2 - 8$  keV band. *Black circles*—remaining sources. The dashed curve shows the Kauffmann et al. (2003) empirical division between star-forming galaxies and AGNs. The dotted curve shows the Kewley et al. (2001) theoretical division.

investigate whether the BPT-comp signal, on average, is dominated by AGN or star formation activity.

Since the BPT diagram is restricted to sources with  $z < 0.5$ , there are too few GOODS-N BPT-comp for a robust stacking analysis (specifically, there are only 22 GOODS-N BPT-comp). To increase our numbers, here we also include the LH galaxy sample. Figure 7 shows the BPT diagram for the 727  $z < 0.5$  GOODS-N/LH galaxies that have [OIII], H $\beta$ , [NII], and H $\alpha$  fluxes with SNR  $> 5$ . We have excluded sources with broadened emission lines (FWHM  $> 2000$  km s $^{-1}$ ) from this analysis.

As discussed in Section 4, the BPT diagnostic does not match 100% with an X-ray selection of AGNs. In Figure 7 we see that 50% (9/18) of the X-ray selected non-BLAGNs with  $L_X > 10^{42}$  erg s $^{-1}$  (black triangles) are BPT-AGN, 28% (5/18) are BPT-comp, and 22% (4/18) are BPT-SF.

In the following sections we do stacking analyses to verify that the remaining  $L_X < 10^{42}$  erg s $^{-1}$  BPT-AGN and BPT-SF are, on average, AGN-dominated and SF-dominated, respectively. Having tested our stacking analyses on these more secure BPT categories, we apply them to our BPT-comp.

### 6.1. X-ray Stacking

Table 3 provides the results from our X-ray stacking analysis for the GOODS-N/LH BPT-SF, BPT-AGN, and BPT-comp. We followed the same procedure as in Section 5.1. We provide specifics for each category in the following subsections.

#### 6.1.1. BPT-SF

There are 605 GOODS-N/LH BPT-SF. Twenty-one are directly X-ray detected. Four of these are obvious X-ray selected AGNs with  $L_X > 10^{42}$  erg s $^{-1}$ . Of the 17

TABLE 3  
 BPT X-RAY STACKING ANALYSIS RESULTS

Category (1)	Total # (2)	# used in stack (3)	$f_{0.5-2}$ keV <sup>a</sup> (4)	$f_{2-8}$ keV <sup>a</sup> (5)	$\langle \Gamma_{\text{eff}} \rangle$ (6)	$z^b$ (7)	$\log L_{2-8}$ keV [erg s <sup>-1</sup> ] (8)
BPT-SF	605	448	$0.66 \pm 0.12$ (5.5 $\sigma$ )	$2.82 \pm 1.23$ (2.3 $\sigma$ )	$1.5_{-0.3}^{+0.7c}$	0.41	40.20 <sup>c</sup>
BPT-AGN <sup>d</sup>	31	17	$5.39 \pm 3.37$ (1.6 $\sigma$ )	$39.4 \pm 22.9$ (1.8 $\sigma$ )	$0.72_{-0.2}^{+1.5e}$	0.41	41.35 <sup>c</sup>
BPT-Comp	91	76	$1.71 \pm 0.33$ (5.2 $\sigma$ )	$8.92 \pm 2.23$ (4.0 $\sigma$ )	$1.0_{-0.4}^{+0.4}$	0.41	40.70

<sup>a</sup>In units of  $10^{-17}$  erg cm<sup>-2</sup> s<sup>-1</sup>.

<sup>b</sup>Volume-weighted redshift for the stacked source.

<sup>c</sup>We caution that this is based on a low significance 2 – 8 keV signal.

<sup>d</sup>Three out of four GOODS-N BPT-AGN and 11 out of 27 LH BPT-AGN are directly detected in their respective *Chandra* image.

<sup>e</sup>Stacking the remaining 17 GOODS-N/LH X-ray undetected BPT-AGN provides poor statistics for the stacking analysis.

<sup>f</sup>We caution that this is based on a low significance 0.5 – 2 keV and 2 – 8 keV signal.

X-ray detected sources with  $L_X < 10^{42}$  erg s<sup>-1</sup>, ten are only detected in the 0.5–2 keV band. Using the 2–8 keV flux limit for their *Chandra* image (see Table 2), we determine an upper limit to their hardness ratios and find that all ten are X-ray soft, with  $\Gamma > 1.7$ . Of the seven remaining sources that are detected in both bands, three are X-ray soft, with  $\Gamma > 1.7$ . Therefore, the majority (13/17) of the X-ray detected,  $L_X < 10^{42}$  erg s<sup>-1</sup> sources are X-ray soft, with  $\Gamma > 1.7$ .

After excluding these known X-ray sources, as well as coincidental contaminants, we use the STACKFAST program to determine the average X-ray signal in the remaining 448 BPT-SF. The stacked source is significantly detected in the 0.5 – 2 keV band (5.5  $\sigma$ ) but not in the 2 – 8 keV band (2.3  $\sigma$ ). We find a  $\langle \Gamma \rangle = 1.5_{-0.3}^{+0.7}$ , although we caution that this is based on a low-significance 2 – 8 keV signal. Given the large uncertainties, the stacked source could be X-ray soft ( $\Gamma > 1.7$ ).

Our MC simulations (see Section 5.1.3 for details of the procedure) yield a 2% probability of randomly generating the observed 0.5 – 2 keV flux for our stacked BPT-SF and a 96% probability of generating the observed 2 – 8 keV flux. Our MC analysis confirms that these BPT-SF clearly have an excess of 0.5 – 2 keV counts, well above those we obtain randomly. The 2 – 8 keV signal is within the noise.

### 6.1.2. BPT-AGN

There are 31 GOODS-N/LH BPT-AGN. Fourteen are directly X-ray detected. Nine of these are obvious X-ray selected AGNs with  $L_X > 10^{42}$  erg s<sup>-1</sup>. Of the five X-ray detected sources with  $L_X < 10^{42}$  erg s<sup>-1</sup>, one is only detected in the 0.5–2 keV band. Using the 2–8 keV flux limit for its *Chandra* image (see Table 2), we determine an upper limit to its hardness ratio and find that it is X-ray soft, with  $\Gamma > 1.7$ . The four remaining sources that are detected in both bands are X-ray hard, with  $\Gamma < 1.4$ .

After excluding these known X-ray sources, as well as coincidental contaminants, we use the STACKFAST program to determine the average X-ray signal in the remaining 17 BPT-AGN. Given the small number of sources in this stacking analysis, it is not surprising that the stacked source is neither significantly detected in the 0.5–2 keV band (1.6  $\sigma$ ) nor in the 2–8 keV band (1.8  $\sigma$ ). We find a  $\langle \Gamma \rangle = 0.72_{-0.2}^{+1.5}$ , although we caution that this is based on a low-significance 0.5 – 2 keV and 2 – 8 keV signal. Given the large uncertainties, this stacked source could be X-ray hard ( $\Gamma < 1.4$ ).

Our MC simulations (see Section 5.1.3 for details of the procedure) yield a  $\sim 98\%$  probability of randomly

generating the observed 0.5 – 2 keV and 2 – 8 keV fluxes. Our MC analysis confirms that the 0.5 – 2 keV and 2 – 8 keV signals are within the noise.

### 6.1.3. BPT-comp

There are 91 GOODS-N/LH BPT-comp. Eleven are directly X-ray detected. Five of these are obvious X-ray selected AGNs with  $L_X > 10^{42}$  erg s<sup>-1</sup>. Of the six X-ray detected sources with  $L_X < 10^{42}$  erg s<sup>-1</sup>, three are only detected in the 0.5–2 keV band. Using the 2–8 keV flux limit for their *Chandra* image (see Table 2), we determine an upper limit to their hardness ratios and find that all three are X-ray soft, with  $\Gamma > 1.7$ . The remaining three sources are detected in both bands and are X-ray hard, with  $\Gamma < 1.4$ .

After excluding known X-ray sources, as well as coincidental contaminants, we use the STACKFAST program to determine the average X-ray signal in the remaining 76 BPT-comp. The stacked source is significantly detected in both bands (5.2  $\sigma$  in the 0.5 – 2 keV band and 4.0  $\sigma$  in the 2 – 8 keV band). We find a  $\langle \Gamma_{\text{eff}} \rangle = 1.0_{-0.4}^{+0.4}$ , i.e., the source is X-ray hard.

Our MC simulations for the BPT-comp yield a 5% probability that we would see the observed 0.5 – 2 keV flux and a 2% probability we would see the observed 2 – 8 keV flux, confirming that we are recovering a real signal in both bands. Fewer than 1% of our MC simulations for the BPT-comp result in both the 0.5–2 keV and 2–8 keV bands detected at a 3  $\sigma$  level or greater. In other words, there is a  $< 1\%$  false-alarm rate for our stacked BPT-comp signal. Thus, the observed X-ray hardness in our BPT-comp appears to be a reliable result.

### 6.2. IR Stacking

As discussed in Section 5.2, the X-ray hard signal in our stacked BPT-comp could be due either to HMXBs or to AGN activity with obscuration. We follow the same procedure as in Section 5.2 to distinguish between these scenarios using the IR. We determine the 1  $\sigma$  error on  $L_X/L_{\text{TIR}}$  for the stacked BPT-comp (gray open diamond) by propagating the errors on both the stacked X-ray and IR signal. Figure 8 shows that the stacked BPT-comp lies  $> 3 \sigma$  above the expected range for  $L_X/L_{\text{TIR}}$  for pure star-forming galaxies (dashed line). This corroborates what we find for the individually X-ray detected BPT-comp (gray filled diamonds), where the majority (8/11) have  $L_X/L_{\text{TIR}}$  values well above the expected range for pure star-forming galaxies. These results support our TBT diagnostic inclusion of the bulk of BPT-comp in the TBT-AGN regime.

We also note that every one of the BPT-AGN, BPT-SF, and BPT-comp with  $L_X > 10^{42}$  erg s $^{-1}$  (large filled symbols) have  $L_X/L_{\text{TIR}}$  values well above the expected range for pure star-forming galaxies. This further confirms that the signal in these X-ray selected AGNs is dominated by AGN activity. An optical classification as BPT-SF is inaccurate.

The stacked BPT-AGN (red open square in Figure 8) was not significantly detected in either the 0.5–2 keV or 2–8 keV bands (1.6  $\sigma$  and 1.8  $\sigma$ , respectively). Nonetheless, we use the derived  $L_X$  from the stacking analysis (see Table 3) and determine the 1  $\sigma$  error on  $L_X/L_{\text{TIR}}$  by propagating the errors on both the stacked X-ray and IR signal. The stacked BPT-AGN  $L_X/L_{\text{TIR}}$  lies well above the expected range for pure star-forming galaxies. This corroborates what we find for the individually X-ray detected BPT-AGN with  $L_X < 10^{42}$  erg s $^{-1}$  (small red filled squares), where the majority (3/5) have  $L_X/L_{\text{TIR}}$  well above the expected range for pure star-forming galaxies. The two with  $L_{\text{TIR}} > 10^{44.5}$  lie within the expected range for pure star-forming galaxies. These two sources are an additional example of the BPT diagnostic potentially misidentifying sources – in this case, SF-dominated sources as BPT-AGN.

The stacked BPT-SF (blue open star in Figure 8) was significantly detected in the 0.5–2 keV band (5.5  $\sigma$ ) but not in the 2–8 keV band (2.3  $\sigma$ ). Nonetheless, we use the derived  $L_X$  from the stacking analysis (see Table 3) and determine the 1  $\sigma$  error on  $L_X/L_{\text{TIR}}$  by propagating the errors on both the stacked X-ray and IR signal. The stacked BPT-SF  $L_X/L_{\text{TIR}}$  is consistent with that expected for pure star-forming galaxies. This corroborates what we find for the individually X-ray detected BPT-SF with  $L_X < 10^{42}$  erg s $^{-1}$  (small blue filled stars), where the majority (12/17) have  $L_X/L_{\text{TIR}}$  values consistent with the expected range for pure star-forming galaxies.

## 7. DISCUSSION – COMPARISON WITH ALTERNATIVE DIAGNOSTICS

As mentioned in the Introduction, Lamareille (2010) investigate the use of a ‘blue diagnostic’ –  $[\text{OIII}]/\text{H}\beta$  versus  $[\text{OII}]/\text{H}\beta$  – to classify galaxies as star-forming galaxies, AGNs, and composites. Although Lamareille (2010) separate out LINERs<sup>7</sup>, here we include both AGNs and LINERs in the BPT-AGN category, as in the rest of our article. Since  $[\text{OIII}]$ ,  $[\text{OII}]$ , and  $\text{H}\beta$  lie at the blue end of the spectrum, this diagnostic can be applied to galaxies with optical spectra out to  $z \sim 0.9$ . This method provides a successful means for creating a reliable sample of star-forming galaxies out to these redshifts. Their SF-dominated regime (SFG in their Table 1) encloses > 99% of the BPT-SF. Only 1.5% of the sources in the SFG regime are BPT-AGN. The ‘blue diagnostic’, however, is not as effective in creating a reliable AGN selection. Their combined Sy2, SF/Sy2, and LINER regimes identify  $\sim 94\%$  of all the BPT-AGN. However,  $\sim 23\%$  of the

<sup>7</sup> The right wing of the BPT diagram further subdivides into an upper and lower branch, with LINERs being the sources in the lower branch exhibiting lower  $[\text{OIII}]$  luminosities (Heckman 1980; Kauffmann et al. 2003). The nature of these sources (weak AGNs versus ‘retired’ galaxies dominated by old stellar populations with relatively hard radiation fields) is still much debated (Kewley et al. 2006; Stasińska et al. 2008; Cid Fernandes et al. 2010, 2011).

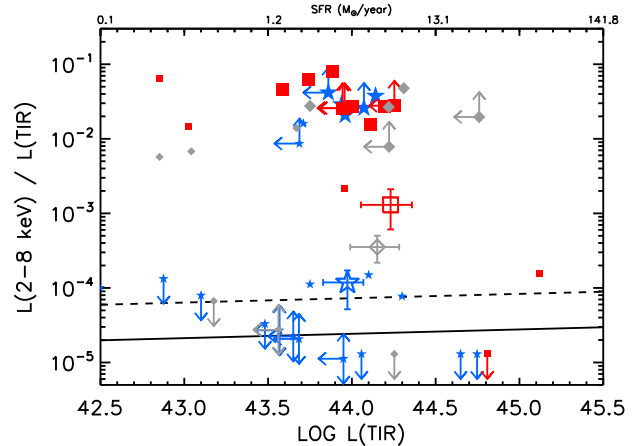


FIG. 8.—  $L_{2-8 \text{ keV}}/L_{\text{TIR}}$  versus  $\log L_{\text{TIR}}$  for our  $z < 0.5$  GOODS-N/LH galaxies that have  $[\text{OIII}]$ ,  $\text{H}\beta$ ,  $[\text{NII}]$ , and  $\text{H}\alpha$  fluxes with  $\text{SNR} > 5$ . Red filled squares – directly X-ray detected BPT-AGN. Blue filled stars – directly X-ray detected BPT-SF. Gray filled diamonds – directly X-ray detected BPT-comp. Large (small) symbols designate sources with  $L_X > 10^{42}$  erg s $^{-1}$  ( $L_X < 10^{42}$  erg s $^{-1}$ ). Downward pointing arrows indicate sources undetected in the 2–8 keV band (but detected in the 0.5–2 keV band) that are assigned the 2–8 keV flux limit (see Table 2). Upward and leftward pointing arrows indicate sources undetected in the *Spitzer* 24 $\mu\text{m}$  image that are assigned the 24 $\mu\text{m}$  flux limit (see Table 2). Blue open star – stacked BPT-SF, excluding directly X-ray detected sources. Red open square – stacked BPT-AGN, excluding directly X-ray detected sources. Gray open diamond – stacked BPT-comp, excluding directly X-ray detected sources. Solid line – expected ratio for the HMXB population in a galaxy with the given SFR (see top axis), according to Persic et al. (2004). Dashed line – expected ratio for the overall star formation occurring in a galaxy with the given SFR, according to Mineo et al. (2011).

sources in this combined regime are BPT-SF<sup>8</sup>.

A classification scheme based on  $[\text{NeIII}]/[\text{OII}]$  (Stasińska et al. 2006; this work) complements this ‘blue diagnostic’ by correctly classifying galaxies in the Lamareille (2010) SF/Sy2 category. Marocco et al. (2011) recently examined the location of the Lamareille (2010) SF/Sy2 galaxies in the Stasińska et al. (2006) DEW diagnostic –  $[\text{NeIII}]/[\text{OII}]$  versus  $D_n[4000]$ . They find that by applying an additional empirical cut in the DEW diagnostic space to these SF/Sy2 galaxies, they are able to correctly identify 99% of the BPT-SF and 97% of the Seyfert 2s. Overall, this combined diagnostic correctly identifies 85% of Seyfert 2s and 99% of BPT-SF.

Our TBT diagnostic, based on  $[\text{NeIII}]/[\text{OII}]$  versus rest-frame  $g - z$  color (rather than  $D_n[4000]$ ), results in minimal overlap between the BPT-SF and BPT-AGN, with only  $\sim 1.3\%$  of the BPT-AGN lying within the TBT-SF regime and only 2.8% of BPT-SF lying within the TBT-AGN regime. Likewise, of the sources in the TBT-AGN regime, only 3.5% are BPT-SF and of the sources in the TBT-SF regime, only 1% are BPT-AGN.

The Juneau et al. (2011) MEx diagnostic –  $[\text{OIII}]/\text{H}\beta$  versus stellar mass – also complements the ‘blue diagnostic’ in its ability to reliably identify AGNs. The MEx-AGN regime encloses 99% of BPT-AGN. Only 6% of the

<sup>8</sup> If we remove the LINER regime from this analysis, we note that the Sy2 and SF/Sy2 regimes enclose 59% and 26% of the Seyferts, respectively. While  $< 3\%$  of sources in the Sy2 regime are BPT-SF, 74% of sources in the SF/Sy2 regime are BPT-SF.



sources in the MEx-AGN regime are BPT-SF. Similarly, the Yan et al. (2011) CEx diagnostic –  $[\text{OIII}]/\text{H}\beta$  versus rest-frame  $U - B$  color – also complements the ‘blue diagnostic’, with the CEx-AGN regime enclosing 95.7% of BPT-AGN. Only 1.9% of the sources in the CEx-AGN regime are BPT-SF.

An important difference between the MEx and CEx diagnostics and our TBT diagnostic is the classification of X-ray selected AGNs. While 8% (8/101) of the Juneau et al. and 22% (30/126) of the Yan et al. X-ray selected  $L_X > 10^{42}$  erg s $^{-1}$  AGNs lie in the MEx-SF and CEx-SF regimes of their diagnostics, respectively, only 3% (3/103) of our X-ray selected AGNs lie within our TBT-SF regime (see Section 4). This may be a result of the higher ionization potential of the  $[\text{NeIII}]$  line (63.45 eV) as compared with the  $[\text{OIII}]$  line (54.94 eV). The higher ionization potential appears to foster a more reliable selection of AGN-dominated galaxies, i.e., the weaker ionizing flux in star-forming galaxies lessens their ability to excite  $[\text{NeIII}]$  as compared to  $[\text{OIII}]$ .

We note that our approach does not address the issue of classifying galaxies with very low equivalent width emission lines, where some of the lines are too noisy for traditional line diagnostics to be used. See Cid Fernandes et al. (2010, 2011) for their discussion of the WHAN diagram –  $W_{\text{H}\alpha}$  versus  $[\text{NII}]/\text{H}\alpha$  – and its ability to provide a more comprehensive emission line classification of galaxies.

#### 7.1. BPT-comp: AGN-dominated sources

A critical difference between the Lamareille (2010) and CEx diagrams and our TBT diagnostic is the location of the BPT-comp (galaxies that fall between the Kauffmann et al. 2003 and Kewley et al. 2001 divisions in the BPT diagram). In the Lamareille (2010) diagram,  $\sim 83\%$  of BPT-comp lie within the SFG regime. In the combined Lamareille (2010) and Marocco et al. (2011) diagnostic,  $\sim 60\%$  of BPT-comp lie within the SFG+SFG/comp regimes. In the CEx diagram,  $\sim 75\%$  of BPT-comp lie within the CEx-SF regime. In our TBT diagnostic, on the other hand, 65% of the BPT-comp lie within the TBT-AGN regime, with only 35% in the TBT-SF regime. Similarly, in the MEx diagnostic (Juneau et al. 2011), only 17% of BPT-comp lie within the MEx-SF regime.

A number of optical emission-line studies have argued that the signal in BPT-comp is dominated by star formation activity, rather than AGN activity. The Kewley et al. (2001) upper boundary to the BPT-comp regime marks their theoretical prediction for galaxies whose contribution from AGN activity to the extreme ultraviolet ionizing radiation field just begins to exceed 50%. According to this work, all sources to the lower-left of this boundary have their signal dominated by star formation activity. Similarly, Stasińska et al. (2006) use spectral synthesis modeling to argue that the contribution from AGN activity to the emission-line signal in BPT-comp is 20% or less. Furthermore, Kewley et al. (2006) note that BPT-comp lie in the same parameter space as HII regions in the  $[\text{OIII}]/[\text{OII}]$  versus  $[\text{OI}]/\text{H}\alpha$  diagnostic (as well as within the SF-dominated regime of the  $[\text{OIII}]/\text{H}\beta$  vs.  $[\text{SII}]/\text{H}\alpha$  diagnostic). They argue that this provides further support for the idea that the ionizing radiation field and ionization parameter in BPT-

comp are dominated by star formation activity.

Here we argue that our TBT diagnostic’s reliance on  $[\text{NeIII}]$ , with its higher ionization potential than  $[\text{OIII}]$ ,  $[\text{NII}]$ , or  $[\text{SII}]$ , leads to a more reliable identification of AGN-dominated sources. In Section 6 we tested whether the inclusion of the majority of BPT-comp in our TBT-AGN regime was justified. Of the individually X-ray detected BPT-comp, 70% are X-ray hard with  $L_X/L_{\text{TIR}}$  ratios indicative of dominance by AGN activity (see Figure 6). The stacked signal from X-ray undetected BPT-comp is also X-ray hard and exhibits an  $L_X/L_{\text{TIR}}$  ratio  $> 3 \sigma$  above the expected range for pure star-forming galaxies. This supports our TBT diagnostic inclusion of BPT-comp in the TBT-AGN regime and suggests that, on average, the X-ray and optical signal in BPT-comp is dominated by AGN activity.

## 8. SUMMARY

We have shown that the TBT diagnostic – rest-frame  $^{0.0}(g - z)$  color versus  $[\text{NeIII}]/[\text{OII}]$  – reliably separates SDSS SF-dominated sources from AGN-dominated sources, as classified according to the classic BPT diagram. Because both  $[\text{NeIII}]$  and  $[\text{OII}]$  are located in the blue end of the optical spectrum, we are able to classify galaxies using this diagnostic out to  $z = 1.4$ . The TBT diagnostic provides a significant extension in redshift compared to the BPT diagram (limited in its use with optical spectra to  $z < 0.5$ ) and the more recent  $[\text{OIII}]/\text{H}\beta$ -based diagnostics (limited to  $z < 0.9$  – ‘blue diagram’, Lamareille 2010, Marocco et al. 2011; CEx, Yan et al. 2011; MEx, Juneau et al. 2011).

We find that the TBT selection of AGNs matches well with an X-ray selection of AGNs, with 97% (100/103) of our OPTX X-ray selected AGNs lying within the TBT-AGN regime. This suggests that the TBT diagnostic is more reliable than the BPT diagnostic in identifying X-ray selected AGNs, since the BPT diagnostic misidentifies  $\sim 20\%$  of our OPTX X-ray selected AGNs as BPT-SF, i.e., as star-forming galaxies. This may be a result of the higher ionization potential of the  $[\text{NeIII}]$  line (63.45 eV) as compared with the  $[\text{OIII}]$  line (54.94 eV). The higher ionization potential appears to foster a more reliable selection of AGN-dominated galaxies, i.e., the weaker ionizing flux in star-forming galaxies lessens their ability to excite  $[\text{NeIII}]$  as compared to  $[\text{OIII}]$ .

We perform X-ray and IR stacking analyses of the GOODS-N sample of galaxies with accompanying deep *Chandra* imaging to verify the dominance of AGN activity in our TBT-AGN and star formation activity in our TBT-SF. We find that the TBT-AGN, on average, are X-ray hard with  $L_X/L_{\text{TIR}} > 3 \sigma$  above the expected range for pure star-forming galaxies. Their X-ray hardness and excess X-ray signal is likely due to obscured or weak AGN activity. The TBT-SF, on the other hand, are X-ray soft with  $L_X/L_{\text{TIR}}$  consistent with pure star-forming galaxies.

We perform the same stacking analyses on the BPT categories in order to confirm the selection of the majority of BPT-comp as TBT-AGN. As expected, the BPT-SF are X-ray soft with  $L_X/L_{\text{TIR}}$  consistent with pure star-forming galaxies and the BPT-AGN are X-ray hard with  $L_X/L_{\text{TIR}} > 3 \sigma$  above the expected range for pure star-forming galaxies. Of the individually X-ray detected BPT-comp, 70% are X-ray hard with  $L_X/L_{\text{TIR}}$



ratios indicative of dominance by AGN activity. Our stacked BPT-comp is significantly detected in both the 0.5 – 2 keV and 2 – 8 keV bands and is X-ray hard, with  $\langle \Gamma_{\text{eff}} \rangle = 1.0_{-0.4}^{+0.4}$ . Furthermore, the stacked BPT-comp  $L_X/L_{\text{TIR}}$  is  $> 3 \sigma$  above the expected range for pure star-forming galaxies. These findings support our TBT diagnostic inclusion of BPT-comp in the TBT-AGN regime.

The BPT-comp (individual and stacked) properties suggest that, on average, both their X-ray and optical signal is dominated by obscured or weak AGN activity. This is in contrast to claims by previous optical emission-line studies that the signal in BPT-comp is dominated by star formation activity. Therefore, we recommend that groups carefully consider the impact of excluding or including BPT-comp on the interpretation of their results. For example, for studies involving determining the bolometric contribution from AGN activity or the role of AGN activity in galaxy evolution, we advise maximal inclusiveness. Since BPT-comp comprise a significant percentage of the overall emission-line galaxy population (20% of the SDSS DR8 sample), inclusion of the BPT-comp would provide a more comprehensive picture of the true impact of AGN activity in these studies.

On the other hand, for metallicity studies of star-forming galaxies, we advise maximal conservativeness (e.g., Tremonti et al. 2004). Emission lines like [OIII] are boosted by AGN activity and can masquerade as indicators of low metallicity, leading to the misinterpretation of results. Therefore, in this case, it is optimal to use a diagnostic that reliably excludes all AGNs and AGN/SF composites.

The authors thank the referee for comments and sug-

gestions which helped to improve this manuscript. We thank Ryan Hickox for helpful discussions and training in the use of his STACKFAST X-ray stacking code. We gratefully acknowledge support from NSF grant AST 0708793, the University of Wisconsin Research Committee with funds granted by the Wisconsin Alumni Research Foundation, and the David and Lucile Packard Foundation (A. J. B.). LT acknowledges support through a CIERA postdoctoral fellowship.

Funding for SDSS-III has been provided by the Alfred P. Sloan Foundation, the Participating Institutions, the National Science Foundation, and the U.S. Department of Energy Office of Science. The SDSS-III web site is <http://www.sdss3.org/>.

SDSS-III is managed by the Astrophysical Research Consortium for the Participating Institutions of the SDSS-III Collaboration including the University of Arizona, the Brazilian Participation Group, Brookhaven National Laboratory, University of Cambridge, University of Florida, the French Participation Group, the German Participation Group, the Instituto de Astrofísica de Canarias, the Michigan State/Notre Dame/JINA Participation Group, Johns Hopkins University, Lawrence Berkeley National Laboratory, Max Planck Institute for Astrophysics, New Mexico State University, New York University, Ohio State University, Pennsylvania State University, University of Portsmouth, Princeton University, the Spanish Participation Group, University of Tokyo, University of Utah, Vanderbilt University, University of Virginia, University of Washington, and Yale University.

We wish to recognize and acknowledge the very significant cultural role and reverence that the summit of Mauna Kea has always had within the indigenous Hawaiian community. We are most fortunate to have the opportunity to conduct observations from this mountain.

## REFERENCES

- Abazajian, K. N., et al. 2009, *ApJS*, 182, 543  
 Aihara, H., et al. 2011, *ApJS*, 193, 29  
 Alexander, D. M., Bauer, F. E., Chapman, S. C., Smail, I., Blain, A. W., Brandt, W. N., & Ivison, R. J. 2005, *ApJ*, 632, 736  
 Alexander, D. M., Brandt, W. N., Hornschemeier, A. E., Garmire, G. P., Schneider, D. P., Bauer, F. E., & Griffiths, R. E. 2001, *AJ*, 122, 2156  
 Alexander, D. M., et al. 2003, *AJ*, 126, 539  
 Baldwin, J. A., Phillips, M. M., & Terlevich, R. 1981, *PASP*, 93, 5  
 Barger, A. J., Cowie, L. L., Brandt, W. N., Capak, P., Garmire, G. P., Hornschemeier, A. E., Steffen, A. T., & Wehner, E. H. 2002, *AJ*, 124, 1839  
 Barger, A. J., Cowie, L. L., & Wang, W.-H. 2008, *ApJ*, 689, 687  
 Bauer, F. E., Alexander, D. M., Brandt, W. N., Hornschemeier, A. E., Vignali, C., Garmire, G. P., & Schneider, D. P. 2002, *AJ*, 124, 2351  
 Bethermin, M., Dole, H., Beelen, A., & Aussel, H. 2010, *VizieR Online Data Catalog*, 351, 29078  
 Blanton, M. R., & Roweis, S. 2007, *AJ*, 133, 734  
 Bongiorno, A., et al. 2010, *A&A*, 510, A56  
 Brandt, W. N., Hornschemeier, A. E., Schneider, D. P., Alexander, D. M., Bauer, F. E., Garmire, G. P., & Vignali, C. 2001, *ApJ*, 558, L5  
 Bruzual, G., & Charlot, S. 2003, *MNRAS*, 344, 1000  
 Cardiel, N., Gorgas, J., & Aragon-Salamanca, A. 1998, *MNRAS*, 298, 977  
 Chabrier, G. 2003, *PASP*, 115, 763  
 Chilingarian, I. V., Melchior, A.-L., & Zolotukhin, I. Y. 2010, *MNRAS*, 405, 1409  
 Cid Fernandes, R., Stasińska, G., Mateus, A., & Vale Asari, N. 2011, *MNRAS*, 413, 1687  
 Cid Fernandes, R., Stasińska, G., Schlickmann, M. S., Mateus, A., Vale Asari, N., Schoenell, W., & Sodré, L. 2010, *MNRAS*, 403, 1036  
 Cohen, J. G., Hogg, D. W., Blandford, R., Cowie, L. L., Hu, E., Songaila, A., Shopbell, P., & Richberg, K. 2000, *ApJ*, 538, 29  
 Coil, A. L., et al. 2009, *ApJ*, 701, 1484  
 Colbert, E. J. M., Heckman, T. M., Ptak, A. F., Strickland, D. K., & Weaver, K. A. 2004, *ApJ*, 602, 231  
 Cooper, M. C., et al. 2011, *ApJS*, 193, 14  
 Cowie, L. L., & Barger, A. J. 2008, *ApJ*, 686, 72  
 Cowie, L. L., Barger, A. J., Hu, E. M., Capak, P., & Songaila, A. 2004, *AJ*, 127, 3137  
 David, L. P., Jones, C., & Forman, W. 1992, *ApJ*, 388, 82  
 Erb, D. K., Shapley, A. E., Pettini, M., Steidel, C. C., Reddy, N. A., & Adelberger, K. L. 2006, *ApJ*, 644, 813  
 Fabbiano, G. 2006, *ARA&A*, 44, 323  
 Fabbiano, G., & Shapley, A. 2002, *ApJ*, 565, 908  
 Faber, S. M., et al. 2003, *Proc. SPIE*, 4841, 1657  
 Fiore, F., et al. 2008, *ApJ*, 672, 94  
 Gehrels, N. 1986, *ApJ*, 303, 336  
 Georgakakis, A., Georgantopoulos, I., Stewart, G. C., Shanks, T., & Boyle, B. J. 2003, *MNRAS*, 344, 161  
 Georgakakis, A., Rowan-Robinson, M., Babbedge, T. S. R., & Georgantopoulos, I. 2007, *MNRAS*, 377, 203  
 Georgantopoulos, I., Georgakakis, A., Rowan-Robinson, M., & Rovilos, E. 2008, *A&A*, 484, 671  
 Giavalisco, M., et al. 2004, *ApJ*, 600, L93  
 Grimm, H., Gilfanov, M., & Sunyaev, R. 2003, *MNRAS*, 339, 793  
 Heckman, T. M. 1980, *A&A*, 87, 152  
 Hickox, R. C., et al. 2007, *ApJ*, 671, 1365

- Hornschemeier, A. E., Brandt, W. N., Alexander, D. M., Bauer, F. E., Garmire, G. P., Schneider, D. P., Bautz, M. W., & Chartas, G. 2002, *ApJ*, 568, 82
- Hornschemeier, A. E., Heckman, T. M., Ptak, A. F., Tremonti, C. A., & Colbert, E. J. M. 2005, *AJ*, 129, 86
- Hornschemeier, A. E., et al. 2001, *ApJ*, 554, 742
- Juneau, S., Dickinson, M., Alexander, D. M., & Salim, S. 2011, *ApJ*, 736, 104
- Kauffmann, G., et al. 2003, *MNRAS*, 346, 1055
- Keenan, R. C., Trouille, L., Barger, A. J., Cowie, L. L., & Wang, W. 2010, *ApJS*, 186, 94
- Kewley, L. J., Dopita, M. A., Sutherland, R. S., Heisler, C. A., & Trevena, J. 2001, *ApJ*, 556, 121
- Kewley, L. J., & Ellison, S. L. 2008, *ApJ*, 681, 1183
- Kewley, L. J., Groves, B., Kauffmann, G., & Heckman, T. 2006, *MNRAS*, 372, 961
- Laird, E. S., Nandra, K., Adelberger, K. L., Steidel, C. C., & Reddy, N. A. 2005, *MNRAS*, 359, 47
- Lamareille, F. 2010, *A&A*, 509, 53
- Lamareille, F., Mouhcine, M., Contini, T., Lewis, I., & Maddox, S. 2004, *MNRAS*, 350, 396
- Lehmer, B. D., et al. 2005, *AJ*, 129, 1
- . 2008, *ApJ*, 681, 1163
- Magnelli, B., Elbaz, D., Chary, R. R., Dickinson, M., Le Borgne, D., Frayer, D. T., & Willmer, C. N. A. 2009, *A&A*, 496, 57
- Marocco, J., Hache, E., & Lamareille, F. 2011, *A&A*, 531, A71
- Mineo, S., Gilfanov, M., & Sunyaev, R. 2011, *Astronomische Nachrichten*, 332, 349
- Moran, E. C., Lehnert, M. D., & Helfand, D. J. 1999, *ApJ*, 526, 649
- Nandra, K., Mushotzky, R. F., Arnaud, K., Steidel, C. C., Adelberger, K. L., Gardner, J. P., Teplitz, H. I., & Windhorst, R. A. 2002, *ApJ*, 576, 625
- Oke, J. B., et al. 1995, *PASP*, 107, 375
- Persic, M., & Rephaeli, Y. 2007, *A&A*, 463, 481
- Persic, M., Rephaeli, Y., Braito, V., Cappi, M., Della Ceca, R., Franceschini, A., & Gruber, D. E. 2004, *A&A*, 419, 849
- Ptak, A., Heckman, T., Levenson, N. A., Weaver, K., & Strickland, D. 2003, *ApJ*, 592, 782
- Ranalli, P., Comastri, A., & Setti, G. 2003, *A&A*, 399, 39
- Remillard, R. A., & McClintock, J. E. 2006, *ARA&A*, 44, 49
- Rieke, G. H., Alonso-Herrero, A., Weiner, B. J., Pérez-González, P. G., Blaylock, M., Donley, J. L., & Marcillac, D. 2009, *ApJ*, 692, 556
- Rola, C. S., Terlevich, E., & Terlevich, R. J. 1997, *MNRAS*, 289, 419
- Rovilos, E., Georgantopoulos, I., Tzanavaris, P., Pracy, M., Whiting, M., Woods, D., & Goudis, C. 2009, *A&A*, 502, 85
- Shi, F., Zhao, G., & Liang, Y. C. 2007, *A&A*, 475, 409
- Silverman, J. D., et al. 2005, *ApJ*, 618, 123
- Stasińska, G., Cid Fernandes, R., Mateus, A., Sodré, L., & Asari, N. V. 2006, *MNRAS*, 371, 972
- Stasińska, G., Vale Asari, N., Cid Fernandes, R., Gomes, J. M., Schlickmann, M., Mateus, A., Schoenell, W., & Sodré, Jr., L. 2008, *MNRAS*, 391, L29
- Szokoly, G. P., et al. 2004, *ApJS*, 155, 271
- Teng, S. H., Wilson, A. S., Veilleux, S., Young, A. J., Sanders, D. B., & Nagar, N. M. 2005, *ApJ*, 633, 664
- Tozzi, P., et al. 2006, *A&A*, 451, 457
- Treister, E., Urry, C. M., & Virani, S. 2009, *ApJ*, 696, 110
- Tremonti, C. A., et al. 2004, *ApJ*, 613, 898
- Tresse, L., Rola, C., Hammer, F., Stasińska, G., Le Fevre, O., Lilly, S. J., & Crampton, D. 1996, *MNRAS*, 281, 847
- Trouille, L., & Barger, A. J. 2010, *ApJ*, 722, 212
- Trouille, L., Barger, A. J., Cowie, L. L., Yang, Y., & Mushotzky, R. F. 2008, *ApJS*, 179, 1
- . 2009, *ApJ*, 703, 2160
- Veilleux, S., & Osterbrock, D. E. 1987, *ApJS*, 63, 295
- Weiner, B. J., et al. 2007, *ApJ*, 660, L39
- Wilkes, B. J., et al. 2009, *ApJS*, 185, 433
- Winter, L. M., Lewis, K. T., Koss, M., Veilleux, S., Keeney, B., & Mushotzky, R. F. 2010, *ApJ*, 710, 503
- Wirth, G. D., et al. 2004, *AJ*, 127, 3121
- Yan, R., et al. 2011, *ApJ*, 728, 38
- Yang, Y., Mushotzky, R. F., Steffen, A. T., Barger, A. J., & Cowie, L. L. 2004, *AJ*, 128, 1501
- York, D. G., et al. 2000, *AJ*, 120, 1579
- Zahid, H. J., Kewley, L. J., & Bresolin, F. 2011, *ApJ*, 730, 137
- Zezas, A. L., Georgantopoulos, I., & Ward, M. J. 1998, *MNRAS*, 301, 915